ATOMS: ALMA three-millimetre observations of massive star-forming regions–XVII. High-mass star-formation through a large-scale collapse in IRAS 15394−5358

Swagat R. Das [1]★, Manuel Merello,[1]★ Leonardo Bronfman,[1]★ Tie Liu,[2] Guido Garay
,[1,3] Amelia Stutz,[4] Diego Mardones,[1] Jian-Wen Zhou [5] Patricio Sanhueza,[6,7,8] Hong-Li Liu [9]
Enrique Vázquez-Semadeni [10] Gilberto C. Gómez [10] Aina Palau [10] Anandmayee Tej,[11]
Feng-Wei Xu,[12,13] Tapas Baug,[14] Lokesh K. Dewangan [15] Jinhua He,[1,3,16] Lei Zhu,[3] Shanghuo Li,[17,18]
Mika Juvela [19] Anindya Saha [11] Namitha Issac [2] Jihye Hwang,[20] Hafiz Nazeer[11] and L. Viktor Toth[21]

[1]*Departamento de Astronomá, Universidad de Chile, Las Condes, 7591245 Santiago, Chile*
[2]*Shanghai Astronomical Observatory, Chinese Academy of Sciences, 80 Nandan Road, Shanghai 200030, China*
[3]*Chinese Academy of Sciences South America Center for Astronomy, National Astronomical Observatories, CAS, Beijing 100101, China*
[4]*Departamento de Astronomá, Universidad de Concepción, Av. Esteban Iturra s/n, Distrito Universitario 160-C, Chile*
[5]*Max-Planck-Institut für Radioastronomie, Auf dem Hügel 69, D-53121 Bonn, Germany*
[6]*Department of Earth and Planetary Sciences, Institute of Science, Tokyo, Meguro, Tokyo, 152-8551, Japan.*
[7]*National Astronomical Observatory of Japan, National Institutes of Natural Sciences, 2-21-1 Osawa, Mitaka, Tokyo 181-8588, Japan*
[8]*Astronomical Science Program, The Graduate University for Advanced Studies, SOKENDAI, 2-21-1 Osawa, Mitaka, Tokyo 181-8588, Japan*
[9]*School of Physics and Astronomy, Yunnan University, Kunming 650091, P. R. China*
[10]*Instituto de Radioastronomía y Astrofísica, Universidad Nacional Autónoma de México, Apdo. Postal 3-72, Morelia, Michoacán 58089, México*
[11] *Department of Earth & Space Sciences, Indian Institute of Space Science and Technology, Thiruvananthapuram 695 547, Kerala, India*
[12]*Kavli Institute for Astronomy and Astrophysics, Peking University, Beijing 100871, P. R. China*
[13]*Department of Astronomy, School of Physics, Peking University, Beijing 100871, P. R. China*
[14]*S. N. Bose National Centre for Basic Sciences, Block-JD, Sector-III, Salt Lake City, Kolkata 700106, India*
[15]*Physical Research Laboratory, Navrangpura, Ahmedabad 380 009, India*
[16]*Yunnan Observatories, Chinese Academy of Sciences, 396 Yang-fangwang, Guandu District, Kunming 650216, P. R. China*
[17]*Max Planck Institute of Astronomy, Königstuhl 17, D-69117 Heidelberg, Germany*
[18]*SOFIA Science Centre, USRA, NASA Ames Research Centre, MS-12, N232, Moffett Field, CA 94035, USA*
[19]*Department of Physics, University of Helsinki, PO Box 64, FI-00014 Helsinki, Finland*
[20]*Korea Astronomy and Space Science Institute, 776 Daedeokdaero, Yuseong-gu, Daejeon 34055, Republic of Korea*
[21]*Institute of Physics and Astronomy, Eotvos Lorand University, Pazmany Peter setany 1/A, H-1117 Budapest, Hungary*

ABSTRACT

Hub-filament systems are considered as natural sites for high-mass star formation. Kinematic analysis of the surroundings of hub-filaments is essential to better understand high-mass star formation within such systems. In this work, we present a detailed study of the massive Galactic protocluster IRAS 15394−5358, using continuum and molecular line data from the ALMA three-millimetre observations of massive star-forming regions (ATOMS) survey. The 3 mm dust continuum map reveals the fragmentation of the massive (M = 843 $M_\odot$) clump into six cores. The core C-1A is the largest (radius = 0.04 pc), the most massive (M = 157 $M_\odot$), and lies within the dense central region, along with two smaller cores (M = 7 and 3 $M_\odot$). The fragmentation process is consistent with the thermal Jeans fragmentation mechanism and virial analysis shows that all the cores have small virial parameter values ($\alpha_{vir} << 2$), suggesting that the cores are gravitationally bound. The mass versus radius relation indicates that three cores can potentially form at least a single massive star. The integrated intensity map of $H^{13}CO^+$ shows that the massive clump is associated with a hub-filament system, where the central hub is linked with four filaments. A sharp velocity gradient is observed towards the hub, suggesting a global collapse where the filaments are actively feeding the hub. We discuss the role of global collapse and the possible driving mechanisms for the massive star formation activity in the protocluster.

Key words: stars: formation – stars: kinematics and dynamics – ISM: clouds – ISM: individual objects: IRAS 15394−5358.

1 INTRODUCTION

High-mass (> 8 $M_\odot$) stars are the powerhouses of galaxies. They play a major role in the formation and evolution of galaxies through their feedback. These high-mass stars also play a central role in

★ E-mail: dasswagat77@gmail.com (SD); mmerello@das.uchile.cl (MM); leo@das.uchile.cl (LB)

synthesizing the chemistry of galaxies. However, the formation mechanism of high-mass stars is still a subject of debate in astrophysics. Formation within the densest regions of molecular clouds, in a complex clustered environment, and the large distances of the massive star-forming regions pose a challenge to studying them observationally.

The 'turbulent core' (McKee & Tan 2003), and 'competitive accretion' (Bonnell et al. 2001; Bonnell, Vine & Bate 2004) theoretical models are frequently considered for explaining the massive star formation process. The 'turbulent core' model is a scaled-up version or extension of the low-mass star formation theory (Shu, Adams & Lizano 1987), proposing a monolithic collapse of high-mass prestellar cores. According to this model, the massive pre-stellar cores are supported against collapse or fragmentation by a significant degree of turbulence and strong magnetic fields. In the 'competitive accretion' model, the massive protostars start with initial Jeans fragmentation. The growth in the mass of the objects happens through Bondi–Hoyle accretion (Vázquez-Semadeni, Gómez & González-Samaniego 2024). In this model, the massive objects need to be near the centre of the gravitational potential well of the molecular cloud so that it favours more accretion with respect to its neighbouring protostellar objects (e.g. Contreras et al. 2018). Apart from these two models, a few more scenarios of massive star formation are also proposed based on observations. For instance, the global hierarchical collapse (GHC) scenario (Vázquez-Semadeni et al. 2009; Vázquez-Semadeni, González-Samaniego & Colín 2017; Vázquez-Semadeni et al. 2019), where gravitationally driven fragmentation occurs in molecular clouds. This model considers the collapse to be hierarchical, suggesting the presence of small-scale within large-scale collapses, where such large-scale accretion is expected to feed the massive star-forming regions. Motte, Bontemps & Louvet (2018) proposed an evolutionary scenario suggesting the high-mass analogues of pre-stellar cores can be replaced by large-scale ($\sim 0.1 - 1$ pc) gas reservoirs, called starless massive dense cores (MDCs) or starless clumps. During their protostellar phase, these mass reservoirs would concentrate their mass into high-mass cores at the same time that stellar embryos would accrete, skipping the high-mass pre-stellar core phase. Padoan et al. (2020) propose the inertial-inflow (IF) model, a scenario where massive stars are assembled by large-scale, converging, inertial flows that naturally occur in supersonic turbulence. According to this model, the mass distribution of stars is primarily the result of turbulent fragmentation under the hypothesis that the statistical properties of turbulence determine the formation time-scale and mass of pre-stellar cores, posing definite constraints on the formation mechanism of massive stars.

Observational studies have shown that a global collapse in molecular clouds towards the potential well happens when mass from the surrounding gets transferred through filaments (e.g. Peretto et al. 2013). The connection of more than three or four filaments with the potential well is usually called a 'hub-filament' system, where the centre of the potential well is the hub. In such a system, the cores within the hubs grow in mass and size by accreting matter from the surrounding environment. The accretion time can be longer while the matter gets funnelled to the hubs. Several studies have revealed that the hub-filament systems are ideal for the formation of high-mass stars and clusters (Peretto et al. 2013; Henshaw et al. 2014; Zhang et al. 2015; Liu et al. 2016; Baug et al. 2018; Lu et al. 2018; Yuan et al. 2018; Issac et al. 2019; Liu, Stutz & Yuan 2019; Dewangan et al. 2020; Kumar et al. 2020; Hwang et al. 2022; He et al. 2023; Liu et al. 2023; Yang et al. 2023). Simulations have shown velocity gradients along filaments, resulting from the inflow of matter into the hubs (Wang et al. 2010; Gómez & Vázquez-

Semadeni 2014; Smith et al. 2016; Padoan et al. 2020; Hwang et al. 2022). A recent study utilizing ATOMS (ALMA Three-millimetre Observations of Massive Star-forming regions; Liu et al. 2020) survey data has identified filamentary structures in the ATOMS targets (Zhou et al. 2022), and reported 'hub-filament' systems in many of these targets while conducting a statistical analysis of the accretion flow along the filaments. Another recent work by Xu et al. (2023) did a detailed study of core feeding from a steady accretion flow from global collapse, that continues down to 1000 au scales (Olguin et al. 2021), in one of the well-known hub-filament systems seen in the protocluster region SDC 335.

Many observational analyses have been carried out to study the accretion flow along the filaments at different scales and mass regimes (Liu et al. 2012; Kirk et al. 2013; Peretto et al. 2013; Stutz & Gould 2016; Lu et al. 2018; Chen et al. 2019; Chung et al. 2019; Liu et al. 2019; Treviño-Morales et al. 2019; Chung et al. 2021; Sanhueza et al. 2021; Li et al. 2022; Redaelli et al. 2022; Olguin et al. 2023; Yang et al. 2023; Pan, Liu & Qin 2024). However, the statistics of such analyses is still minimal, and it requires much more attention. High-mass star formation through such a mechanism would be better understood if we probe the kinematics of the surrounding environment of the hub-filament systems. To complement earlier studies of massive star formation in hub-filament systems, in this work, we conduct a detailed kinematic analysis of the protocluster IRAS 15394−5358. This massive protocluster hosts a hub-filament system (Zhou et al. 2022). Our objective is to explore the massive star formation within the hub-filament system of the protocluster by conducting a comprehensive kinematic analysis. Through detailed examination of the kinematics, including velocity dispersion, line profiles, and spatial distributions, we aim to elucidate the mechanisms driving the formation and evolution of high-mass stars within the complex environment of the hub-filament system. This analysis will contribute to a deeper understanding of the processes involved in massive star formation and the role of hub-filament systems in shaping the stellar population of protoclusters. In the following, we provide a brief detail of the massive protocluster.

1.1 Details of protocluster IRAS 15394−5358

The object IRAS 15394−5358 ($l = 326.47$ and $b = 0.70$) has been observed in CS (Bronfman, Nyman & May 1996) and ^{13}CO (Urquhart et al. 2007) line emission. Association with H_2O (Scalise, Rodriguez & Mendoza-Torres 1989) and 6 GHz CH_3OH (Caswell 1998) masers are also observed towards the target. The detection of masers confirms the massive star formation activity in this object. As part of a survey, Faúndez et al. (2004) detected the 1.2 mm continuum emission from the protocluster. These authors derived several physical parameters for the object using the kinematic distance of 2.8 kpc. With 1.2 mm dust continuum observation from SEST-SIMBA, Garay et al. (2007) detected a massive dense clump (G326.474 + 0.697) with mass of 1.5×10^3 $M_\odot$ and radius of 0.22 pc, adopting distance of 2.8 kpc. Despite being luminous (5.4×10^3 $L_\odot$; Urquhart et al. 2018), no radio emission was detected towards the object (Garay et al. 2006). Probably, the ionizing source(s) is in the very early stage of evolution, deeply embedded and not revealed yet. The association of extended green objects (EGOs) with IRAS 15394−5358 also indicates an early stage of evolution (Cyganowski et al. 2008). Caratti o Garatti et al. (2015) present the NIR imaging (H_2 and K_s) and spectroscopic (0.95–2.50 µm) analysis of IRAS 15394−5358 and detect the association of a small cluster of young stellar objects (YSOs). These authors reported the association of multiple outflows from continuum subtracted H_2 images. From ATLASGAL 870 µm

emission, Urquhart et al. ([2018](#)) detected a single dust clump towards the *IRAS* object and derived its physical properties. They reported the clump radius to be of 0.5 pc, dust temperature to be 20.7 K, and V_{LSR} of -41.6 km s^{-1}. The dust temperature was derived by conducting a greybody fit to the submillimetre (sub-mm) dust emission, including from *Herschel* 70 μm to ATLASGAL 870 μm. Adopting the distance of 1.8 kpc, they obtained $L_{bol} = 5.4 \times 10^3$ L$_\odot$ and M $= 843.3$ M$_\odot$. The higher mass obtained by Garay et al. ([2007](#)) could be primarily attributed to the higher distance, i.e. 2.8 kpc they adopted. In a later study, Lumsden et al. ([2013](#)) provided this object's parallax distance of 1.8 kpc. In this work, we adopt the later and updated distance estimation of 1.8 kpc for this source.

In Fig. [1](#)(a), we show the two colour-composite image (24 μm – red and 8 μm – green) of the region towards IRAS 15394−5358. This displays a large view of the region around the target. The 8 μm reveals a large dark filamentary structure, where the protocluster is located. Two bright blobs appear in 24 μm emission. The brighter 24 μm blob is associated with the 70 μm point source, suggesting it is more evolved. The 6 GHz CH$_3$OH maser is linked to the less bright 24 μm blob and to two EGOs in its close vicinity. This 24 μm emitting source is less evolved but associated with massive star formation. Fig. [1](#)(b) displays the zoom-in view of the white box area of (a). In this close-up view of 8 μm emission, we can see the extended structures, which appear dark, seen to be extending from the massive dense core. We show the cold dust emission traced by ATLASGAL 870 μm in cyan contours. This cold dust emission reveals a single clump. The CH$_3$OH maser is located within the clump's peak. The white circle shown in this figure is the ALMA field of view, and this work is focused on that region.

In this work, we use data from the ATOMS survey and conduct a detailed analysis of the fragmentation and gas kinematics, and probe the high-mass star formation through a large-scale collapse in the massive Galactic clump IRAS 15394−5358. This work is arranged as follows. We describe the details of data sets in Section [2](#). This includes the details of ALMA observations and archival data sets. We present results in Section [3](#). These includes the results obtained from ALMA 3 mm dust continuum emission and the molecular line emissions. The details of the star formation activity of the protocluster region are provided in Section [4](#). The nature of mass inflow through the filaments and the massive star formation through a large-scale collapse is discussed in Section [5](#). We summarize the results in Section [6](#).

2 OBSERVATIONS AND ARCHIVAL DATA

2.1 ALMA observations

We use the ALMA data from the ATOMS survey (Project ID: 2019.1.00685.S; PI: Tie Liu; Liu et al. [2020](#)). As part of the ATOMS survey, 146 massive *IRAS* clumps were observed in the single-pointing mode with both the Atacama Compact 7 m and the 12 m array configurations in band 3. This survey aims to systematically investigate the spatial distribution of various dense gas tracers (e.g. HCO$^+$, HCN, and their isotopologues), high-mass core (HMC) tracers (e.g. CH$_3$OH and HC$_3$N), shock tracers (e.g. SiO and SO), and ionized gas tracers (H$_{40\alpha}$) in a large sample of Galactic massive clumps. The 146 sources in the ATOMS sample were selected from the CS J $= 2 - 1$ survey of Bronfman et al. ([1996](#)). In this work, we use data from the 12 m plus 7 m array data sets from this survey. Complete details regarding source selection, observations, and data reduction of the ATOMS survey can be found in Liu et al. ([2020](#)). The synthesized beam size and *rms* noise level for the continuum image

are 2.34 arcsec × 2.1 arcsec and 0.4 mJy beam^{-1}, respectively. The synthesized beam sizes for the molecular line data sets range from 2.4 arcsec × 2.1 arcsec to 2.7 arcsec × 2.4 arcsec and the *rms* noise levels range from 0.12 to 9.5 mJy beam^{-1}. The H^{13}CO$^+$ $(1-0)$ line, which is used to study the kinematics of the protocluster has beam size and *rms* noise level of 2.7 arcsec × 2.4 arcsec and 0.12 mJy beam^{-1}, respectively. The data set has a maximum recoverable scale of 81.8 arcsec.

2.2 Archival data

We also use mid-infrared (MIR) to sub-mm archival data sets to study the interaction of the clump with its surrounding environment. We use the MIR images of the GLIMPSE survey (Benjamin et al. [2003](#)), obtained using the *Spitzer* infrared array camera (IRAC) with wavelengths of 3.6, 4.5, 5.8, and 8.0 μm, with a resolution smaller than 2 arcsec. These images trace emission from point sources at shorter wavelengths and warm dust emission at longer wavelengths. The 870 μm sub-mm image from the ATLASGAL survey (Schuller et al. [2009](#)) obtained with the Large APEX Bolometer Camera (LABOCA) is also used in this work. The image has a resolution of 19 arcsec and traces emission from cold dust. We also use the target region's column density and dust temperature maps, generated with the PPMAP procedure (Marsh et al. [2017](#)) using the far-infrared (FIR) data obtained from the *Herschel* Infrared Galactic plane survey (Molinari et al. [2010](#), [2016](#)). The resulting column density and dust temperature maps have ~ 12 arcsec resolutions and are available in the online archive.[1]

3 RESULTS

3.1 Dust continuum emission

3.1.1 Spatial distribution

The emission from the cold dust at 870 μm appears as a single clump. However, the ALMA image at a higher angular resolution of ~ 2.5 arcsec can decipher and unfurl the clump's underlying core structures. In Fig. [2](#), we show the 3 mm continuum map with its contours overlaid. Above the 3σ level, the emission shows a central core with a diffuse, filamentary extension to the southeast harbouring two compact cores. With proper contrast, the central core also reveals the presence of substructures. Another separate core is also visible above the central core. These subsequent cores within the clump indicate the ongoing fragmentation within the massive clump. We match the morphology of the 3 mm continuum emission with the *Spitzer* image shown in Fig. [1](#). The central dense core of the 3 mm continuum map is associated with the less bright 24 μm blob along with the EGOs (Cyganowski et al. [2008](#)), and the 6 GHz CH$_3$OH maser (Caswell [1998](#)). This indicates that the region surrounding the central core is associated with high-mass star formation at an early stage of evolution. The other two brighter cores in the southeast direction are associated with the brighter 24 μm region. Thanks to ALMA's sensitivity and resolution, we can retrieve the cores within it, that appear as a single object at the MIR wavelengths. The massive core is associated with a 70 μm point source. Thus, the two cores are more evolved compared to the central core. We use this 3 mm dust continuum map to identify and derive the physical properties of the cores.
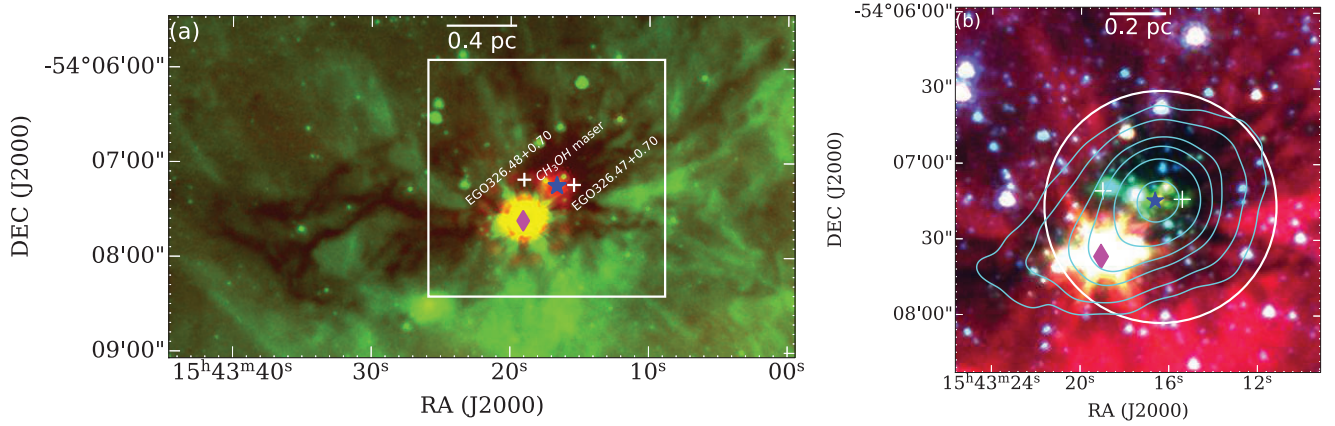
---

[1] http://www.astro.cardiff.ac.uk/research/ViaLactea/

Figure 1. (a) Two colour composite image (24 µm – red and 8 µm – green) of the region towards IRAS 15394−5358. This image shows a larger field of view of the surrounding area of the star-forming region, which lie on the large IRDC. The white box covers a close region around IRAS 15394−5358. (b) Three colour-composite image (8 µm – red, 4.5 µm – green, and 3.6 µm – blue) of the white box region shown in (a). The white circle (radius = 0.7 arcmin) is the ALMA field of view. The cyan contours are emissions at 870 µm from the ATLASGAL survey. The contour levels are 0.6, 1, 2, 3, 5, and 10 Jy beam^{-1}. Different objects towards the region found in the literature are shown in different symbols. The white ' + ' marks are for the EGOs (Cyganowski et al. 2008), the blue star shows the location of 6 GHz CH$_3$OH maser (Caswell 1998), and the magenta diamond for the position of the 70 µm point source. Scale bars of both images are shown on top of each frame.
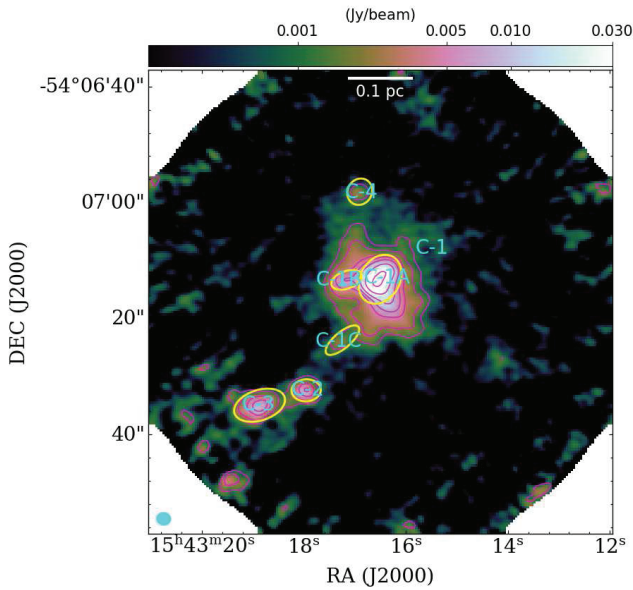

Figure 2. The 3 mm continuum map of the protocluster observed as part of the ATOMS survey is shown in colour. The magenta contours are from the same map with contour levels of 3, 5, 10, 15, 25, and 50 times the noise σ, where $\sigma = 0.0004$ Jy beam^{-1}. The yellow ellipses, along with labels, are the identified cores. A scale bar of 0.1 pc is shown on the top, and the beam size is in the bottom left corner.

3.1.2 Core identification

The ATOMS 3 mm continuum map reveals cores and thus allows their identification. We follow a similar approach of core identification discussed in Li et al. (2020) and applied by other works (Liu et al. 2021; Saha et al. 2022). We use *astrodendro* algorithm (Rosolowsky et al. 2008), and the CASA-*imfit* task to identify the cores and derive their properties. The *astrodendro* algorithm decomposes the map into tree structures such as trunks, branches, and leaves. Leaves are the smallest structures, which are called cores. The *astrodendro* algorithm requires a threshold flux level, a minimum delta value

(contour separation), and the number of pixels to decompose the map into different structures. We use the threshold flux as 1 mJy beam^{-1} (3σ) and the minimum delta as σ. To ensure proper detection of cores, we choose the number of pixels equivalent to the synthesized beam area in pixel units. These parameters are adopted after multiple trials for the robust detection of cores. As discussed in Liu et al. (2021), we first use the *astrodendro* to identify the cores and get their parameters such as core position, major and minor axes sizes, peak and integrated flux, and position angle. In the next step, we use the parameters obtained from *astrodendro* as an initial guess to obtain a more accurate estimation using the CASA *imfit*. Fig. A1 displays the residual map obtained from the task. Following the said procedure, we identified six cores towards IRAS 15394−5358 (see Fig. 2). Three cores are detected in the central part (C-1A, C-1B, C-1C), two (C-2, C-3) towards the southeast of the central core, and the other one (C-4) towards the north of the central core. We called the central region encompassed within the 3σ contour level as core C-1. Cores C-1A, C-1B, and C-1C are the substructures of core C-1. A few dense clumpy structures are seen towards the edges of the map. However, we did not consider them because of the higher uncertainty at the edges of the map. The derived core properties are listed in Table 1. In the residual map (Fig. A1), a bright region emerges to the south of the central core C-1A. Most likely, this is a low-mass core that is not visible in the original map due to the dominance of C-1A but becomes apparent in the residual map.

3.1.3 Physical properties of cores

We derive several physical properties (such as mass, radius, and surface density) of the cores. We estimate the mass of each core using the equation (B1) of Liu et al. (2021),

$$M_{\text{core}} = \frac{F_\nu^{\text{int}} \, R_{\text{gd}} \, D^2}{B_\nu(T_\text{d}) \, \kappa_\nu}, \tag{1}$$

where F_ν^{int} is the integrated flux density obtained for each core from CASA-*imfit*, R_{gd} is the gas-to-dust ratio assumed to be 100, D is the distance to the target source, B_ν is the Planck's function evaluated at dust temperature T_d, and κ_ν is the opacity assumed to be 0.18 cm^2 g^{-1}

Table 1. Physical properties of the cores derived from the 3 mm continuum map.

Name	RA (2000)	DEC (2000)	Decon. FWHM (arcsec × arcsec)	PA (degree)	Peak Flux (mJy beam^{-1})	Int. Flux (mJy)	V_{LSR} (km s^{-1})	T_d (K)	R_{core} (pc)	M_{core} (M$_\odot$)	Σ_{core} (g cm^{-2})	α_{vir}
C-1A	15:43:16.55	−54:07:13.61	4.46 × 3.41	153.0	48.3 ± 3.0	201.0 ± 15.0	−40.0 ± 3.0	23.5 ± 0.4 (39.1 ± 0.02)	0.04	271 ± 155 (157 ± 90)	14.8 ± 8.5 (8.6 ± 4.9)	0.07 (0.12)
C-1B	15:43:17.21	−54:07:13.72	2.75 × 1.51	108.0	4.62 ± 0.32	8.87 ± 0.89	−42.4 ± 1.3	23.5 ± 0.4 (39.1 ± 0.02)	0.02	12 ± 7 (7 ± 4)	2.4 ± 1.4 (1.5 ± 0.8)	0.54 (0.93)
C-1C	15:43:17.29	−54:07:24.12	3.59 × 1.39	128.0	1.91 ± 0.31	4.32 ± 0.98	−42.6 ± 0.9	23.5 ± 0.4 (39.1 ± 0.02)	0.02	6 ± 3.5 (3.4 ± 2.1)	0.9 ± 0.5 (0.6 ± 0.3)	0.01 (0.01)
C-2	15:43:18.00	−54:07:32.76	2.52 × 1.90	93.0	6.77 ± 0.53	13.5 ± 1.5	−42.6 ± 0.1	25.1 ± 0.5	0.02	17 ± 10	2.9 ± 1.7	0.35
C-3	15:43:18.91	−54:07:35.32	4.54 × 2.62	108.0	7.69 ± 0.47	27.1 ± 2.1	−42.0 ± 7.0	25.1 ± 0.5 (46.8 ± 0.1)	0.03	34 ± 19.5 (17.5 ± 10)	2.4 ± 1.4 (1.2 ± 0.7)	0.49 (0.94)
C-4	15:43:16.95	−54:06:58.52	3.14 × 2.54	145.0	2.08 ± 0.26	5.5 ± 0.92	−41.5 ± 0.1	19.5 ± 0.8	0.03	9 ± 5	0.9 ± 0.5	0.30

Note. Values in parentheses are obtained with the revised temperature estimation from the 70 μm flux density (see Section 3.1.3). These revised values are used for further analysis of these cores in this work.

(Ossenkopf & Henning 1994). Urquhart et al. (2018) have mentioned the value of $T_d = 20.7$ K for the whole ATLASGAL clump. For a better estimate of each core's T_d value, we use the dust temperature map generated from *Herschel* images (Marsh et al. 2017). All cores except core (C-4; $T_d = 20$ K) have similar T_d values ($\sim 23 - 25$ K). It is to be noted that the ALMA ATOMS image and the dust temperature map from *Herschel* maps have different resolutions and different pixel sizes. So, an exact comparison between both maps cannot be incorporated.

The surface density (Σ_{core}) is derived using the expression $\Sigma_{core} = M_{core}/\pi R_{core}^2$. We present values of all the physical parameters in Table 1. C-1A is the most massive and the largest among all the cores. This core holds a mass of ~ 270 M$_\odot$ within a radius of 0.04 pc. We also derive the physical properties of core C-1. Since for C-1, we do not have information of deconvolved size from CASA $-$ *imfit*, we derive its physical radius assuming the core to be circular and using the expression $r = (A/\pi)^{0.5}$, where A is the area of the core. The C-1 core's derived mass, radius, and surface density are 372.5 ± 212 M$_\odot$, 0.08 pc, and 3.9 ± 2.2 g cm^{-2}, respectively. The mass of core C-1 is similar to the collective mass of cores C-1A, C-1B, and C-1C.

In a protocluster complex, the temperatures estimated for the cores from the dust temperature map using *Herschel* images might be an underestimation. To obtain more realistic temperature information, Anderson et al. (2021) derived temperatures using the flux density obtained from the Hi-GAL 70 μm Compact Source Catalogue for cores associated with a 70 μm point source. This is because the 70 μm flux density is considered as a good tracer of the luminosity of embedded sources (Dunham et al. 2008; Ragan et al. 2012). In this estimation, the 70 μm flux density is converted into bolometric luminosities (Elia et al. 2017), and the dust temperature is then derived under the assumption that dust emission from a protostellar core is optically thin and predominantly in the FIR.

Here, we follow the same approach, deriving the temperatures of the central core C-1 and core C-3, as they are associated with 70 μm point sources. The derived dust temperatures are 39.1 ± 0.02 K and 46.8 ± 0.1 K for C-1 and C-3, respectively. As C-1 contains three substructures, the same temperature is considered for the substructures. These derived temperatures of the cores are higher than the temperatures estimated from the dust temperature maps.

With the new temperatures, we derived the physical parameters of these cores, which are listed in Table 1 within parentheses, are used for the remainder of the analysis. The derived mass and surface density of C-1 are 214 ± 121.6 M$_\odot$ and 2.2 ± 1.3 g cm^{-2}, respectively. The cores C-1 and C-3 in our work correspond to the cores MM1 and MM2 in the work of Anderson et al. (2021), whose derived masses are approximately twice as high as ours. In their study, they used a similar image at $\sim$3 mm. The other cores in our work are also relatively less massive compared to those derived by Anderson et al. (2021). The primary reasons for this difference are the varying distance values, opacity, and dust temperatures used in the respective studies. In our work, we adopt a distance of 1.82 kpc, whereas Anderson et al. (2021) used a higher distance of 2.61 kpc. Nevertheless, given the high uncertainties associated with these derived physical parameters, the mass estimates in both the studies agree within their error limits.

3.1.4 Uncertainties in the physical parameters

The parameters of distance and dust temperature can introduce uncertainties in the determination of the physical properties of the cores. In the case of our protocluster, we have a parallax distance estimation of 1.8 kpc (Lumsden et al. 2013). As there are no

reported errors on the distance, we have not factored them into our calculations. The estimation of dust temperature is also subject to variability, influenced by factors such as the characteristics of dense cores and whether they host any hot cores and ultracompact H II (UC H II) regions. We have not detected any H$_{40\alpha}$ emission towards the protocluster, and previous ATOMS studies have not reported any association of hot cores and UC H II regions with the protocluster (Liu et al. 2021; Zhang et al. 2023). Consequently, the currently adopted dust temperature values for the cores are presumed to accurately represent their true nature. However, it's worth noting that considering higher temperatures, such as 100 K, would result in a reduction in core masses by a factor of four to five times.

Additionally, uncertainties in κ_ν and R_{gd} significantly affect the uncertainty of mass and surface density estimates for the cores. In our current calculations, we have adopted a value of κ_ν as 0.18 cm^2 g^{-1}. This opacity value, as described in Liu et al. (2021), is assumed at a frequency of approximately 94 GHz, derived from the 'OH5' dust model. The 'OH5' model is a composite of dust properties from Ossenkopf & Henning (1994) and Pollack et al. (1994), extended towards longer wavelengths by Young & Evans (2005). While models from Ossenkopf & Henning (1994) have been predominantly favoured in multiwavelength studies of star-forming regions (e.g. Shirley et al. 2011), it's important to note that κ_ν remains one of the least precisely known parameters due to challenges in characterizing dust properties.

As discussed in other studies (e.g. Sanhueza et al. 2017, 2019), we have also explored the literature for the potential range of κ_ν. Values for κ_ν at ALMA band 3 range from 0.1 cm^2 g^{-1}, derived using formulations from Marsh, Whitworth & Lomax (2015) and Marsh et al. (2017), to 0.5 cm^2 g^{-1} from the study by Lin et al. (2021), assuming a standard gas-to-dust ratio of 100. As outlined in Sanhueza et al. (2017), if we assume a uniformly distributed range for κ_ν, then the standard deviation is ~ 0.1, corresponding to an error of ~ 50 per cent on the adopted value in this work. A 50 per cent error on κ_ν has also been reported in Roy et al. (2014) and Anderson et al. (2021).

The next parameter that significantly contributes to the uncertainty in mass estimation is the gas-to-dust ratio, R_{gd}. The value of Galactic R_{gd} varies between 70 and 162, depending on factors such as grain size, shape, and compositions (Devereux & Young 1990; Vuong et al. 2003; Draine 2011; Peters et al. 2017). Assuming R_{gd} follows a uniform distribution, the standard deviation is 27, implying an uncertainty of 27 per cent on the adopted value of 100.

Taken together, the uncertainties in both κ_ν and R_{gd}, along with the error in other parameters, result in an overall uncertainty of ~ 60 per cent on the estimates of mass and surface density for the cores. These uncertainties in mass and surface densities are also presented in Table 1.

3.2 Molecular line emission

To get overall properties of the protocluster, we retrieve the average spectra of optically thick line HCO$^+$ (1 − 0) and optically thin line H^{13}CO$^+$ (1 − 0) within the 25 arcsec region around the central position. Due to their high critical density ($\sim 6 \times 10^4$ cm^{-3}; Shirley 2015), both lines are ideal for studying the dense gas properties. Also, the optically thick line, HCO$^+$, can probe the infall and outflow signatures within the cloud. In Fig. 3, we show the average spectra of both line transitions. Both lines show a single emission peak, where the intensity of optically thick HCO$^+$ is approximately five times higher compared to the optically thin H^{13}CO$^+$. The higher
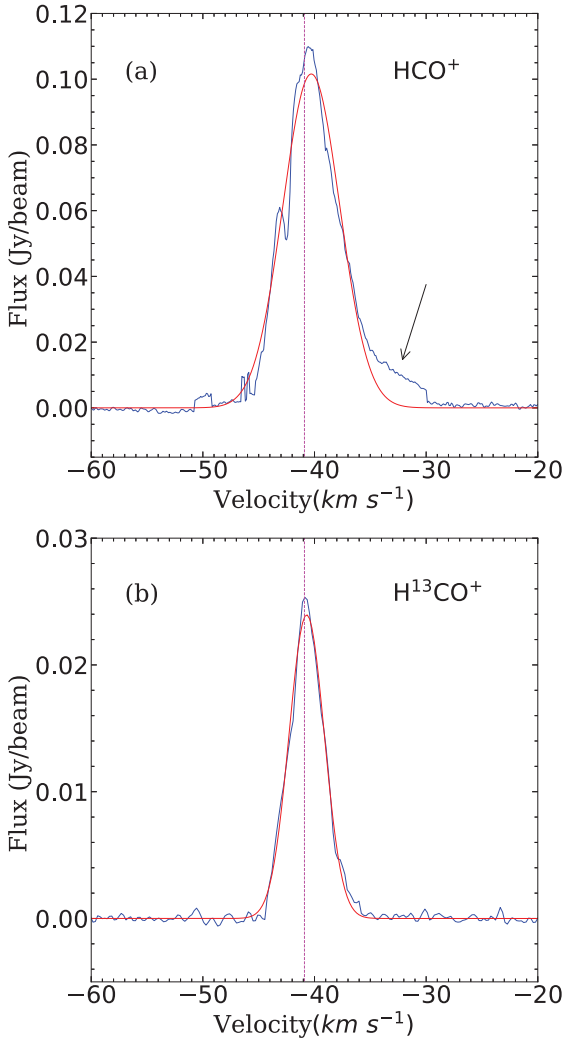
Figure 3. Spectra of HCO$^+$ and H^{13}CO$^+$ lines averaged within 25 arcsec around the centre. The red curves are the Gaussian fitting to the spectra done with `PySpecKit` package (Ginsburg et al. 2022). The vertical straight line in both panels marks the LSR velocity of -40.9 km s^{-1} obtained from CS$(2-1)$ molecular line transition (Bronfman et al. 1996). The arrow in (a) points to the broad line wing in HCO$^+$.

intensity of HCO$^+$ compared to H^{13}CO$^+$ can be attributed to both the abundance variation and the opacity effects of these isotopologues.

Gaussian fitting shows the LSR velocity to be -40.3 and -40.7 km s^{-1} for HCO$^+$ and H^{13}CO$^+$, respectively. This is similar to -40.9 km s^{-1} obtained with CS$(2-1)$ line (Bronfman et al. 1996). Velocity widths are 2.25 and 1.47 km s^{-1} for HCO$^+$ and H^{13}CO$^+$, respectively. The HCO$^+$ spectra show a small dip at ~ -43 km s^{-1} and broad line wings, mainly on the redshifted side. These features indicate a possible outflow in the protocluster region regulated by massive star formation activity. The central hub (C-1) hosts the most massive core and preferentially forms massive star(s), which is discussed later. Hence, we discuss the kinematics of the central hub of this protocluster complex in a later section. The different molecular lines can reveal the central hub's infall/outflow characteristics.

3.2.1 Spatial distribution

Fig. 4 presents the integrated intensity (moment0) maps for ten molecules, showing the morphological features of the line emissions

in the protocluster region IRAS 15394$-$5358. We do not present H$_{40\alpha}$ because there is no detected emission in that line transition, consistent with previous studies (Garay et al. 2006). H^{13}CO$^+$ traces emission from the dense central region with little extended emission in the surroundings. A very faint emission is seen towards the cores C-2 and C-3. The morphology of H^{13}CN and HC$_3$N is similar. Both these lines show enhanced emission towards the massive dense core C-1, with little diffuse emission in the direction of cores C-2 and C-3. CH$_3$OH shows emission from the dense core, with no diffuse emission in the surrounding area. HCN, HCO$^+$, CCH, SiO, CS, and SO reveal much more extended emissions. Emission of CCH, which is a good tracer of photo dissociation region (PDR), shows much more uniform extended emission. Faint emission is seen in the central massive dense core region and towards the other southern cores. This could be due to the presence of H II regions generating PDRs around them. The morphology of SiO is extended with multiple elongated compact structures. These could be the outflows observed towards IRAS 15394$-$5358. A few of such features are also seen in the emissions of HCN and HCO$^+$.

3.2.2 Similarity and differences between molecules

The spatial distribution of the emission in the molecular line transitions (Fig. 4) shows similarities and differences. Since the different transitions trace different physical conditions, it is worth analysing their similarities and differences, allowing us to find the best tracers for different structures within the clouds. We use the principal component analysis (PCA) to conduct such study. Because of the robustness in finding the similarities and differences between line transitions, the PCA has been widely used in studying molecular clouds (Lo et al. 2009; Jones et al. 2012, 2013; Liu et al. 2020). PCA is part of an unsupervised machine learning algorithm, which describes the multidimensional data set through a linear combination of uncorrelated variables called the principal components (PCs). These PCs represent the variances that capture the most significant common features in the data. The PC with the largest variance identifies the most significant feature. Mathematically, PCs are derived by performing eigenvalue decomposition on the covariance matrix (or correlation matrix) of the input variables, resulting in eigenvectors (PCs) and their corresponding eigenvalues, which quantify the variance explained by each PC. We use the SCIKIT-LEARN[2] package of Python to derive the correlation matrix and the variances of the PCs. We analyse this using the integrated intensity maps shown in Fig. 4. As described in Liu et al. (2020), all the maps are smoothed and re-gridded, so all maps have the same resolution and pixel sizes. Before running the analysis, data standardization was performed, resulting in the data having a mean value of zero and a standard deviation of one. This process mitigates the effect of brighter pixels. In this analysis, we used all pixels from the integrated intensity maps of all the molecules. However, we tested the impact of missing zero-spacing data or negative pixels in the analysis by considering the pixels above 3σ for individual molecules. We verified that the presence of missing zero-spacing data or negative pixels in the integrated intensity maps does not alter the final outcome of the analysis.

Table 2 presents the correlation matrix, eigenvalues, and eigenvectors (PCs). In the correlation matrix, a correlation coefficient
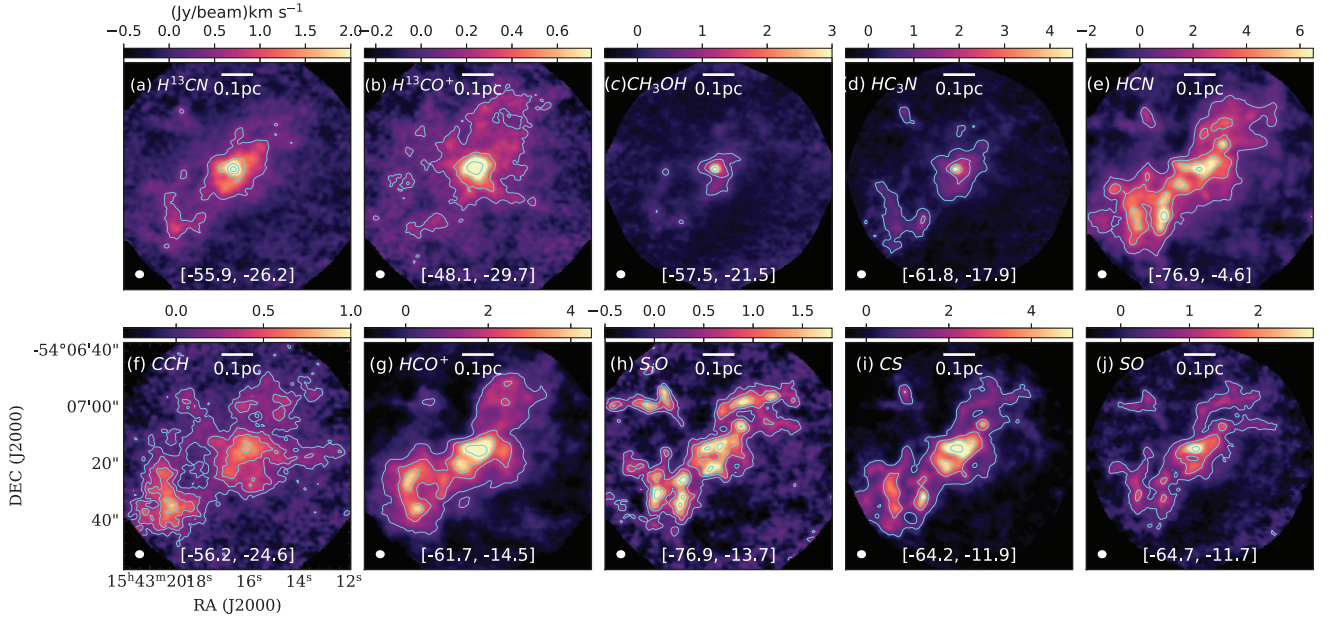
Figure 4. Integrated intensity (moment0) maps of the molecules are displayed. The contours on each panel are from the same map. The contour levels are 10, 30, 50, and 80 per cent of the peak flux. The peak values are 4.60, 1.13, 4.70, 5.30, 9.22, 0.90, 6.30, 2.33, 7.84, and 4.23 (Jy beam^{-1})km s^{-1} for H^{13}CN, H^{13}CO$^+$, CH$_3$OH, HC$_3$N, HCN, CCH, HCO$^+$, SiO, CS, and SO, respectively. A scale bar of 0.1 pc and the beam size are shown on each panel. The numbers within square brackets in all panels give the velocity range over which the lines are integrated.

Table 2. Results of PCA analysis.

	H^{13}CN	H^{13}CO$^+$	CCH	SiO	HCN	HCO$^+$	CH$_3$OH	HC$_3$N	CS	SO
H^{13}CN	1.00	**0.88**	0.76	0.79	**0.84**	**0.86**	**0.80**	**0.94**	**0.92**	**0.90**
H^{13}CO$^+$	**0.88**	1.00	0.70	0.62	0.70	0.76	0.68	**0.81**	0.77	0.77
CCH	0.76	0.70	1.00	0.64	**0.80**	**0.84**	0.44	0.76	**0.81**	0.66
SiO	0.79	0.62	0.64	1.00	**0.87**	0.78	0.59	0.77	**0.84**	**0.91**
HCN	**0.84**	0.70	**0.80**	0.87	1.00	**0.94**	0.54	**0.80**	**0.93**	**0.85**
HCO$^+$	**0.86**	0.76	**0.84**	0.78	**0.94**	1.00	0.58	**0.82**	**0.93**	**0.83**
CH$_3$OH	**0.80**	0.68	0.44	0.59	0.54	0.58	1.00	**0.81**	0.67	0.77
HC$_3$N	**0.94**	**0.81**	0.76	0.77	**0.80**	**0.82**	**0.81**	1.00	**0.91**	**0.88**
CS	**0.92**	0.77	**0.81**	**0.84**	**0.93**	**0.93**	0.67	**0.91**	1.00	**0.90**
SO	**0.90**	0.77	0.66	**0.91**	**0.85**	**0.83**	0.77	**0.88**	**0.90**	1.0

Correlation matrix values of the data set

Eigen values and eigen vectors or contributions of each line in the directions of principal components

Component	1	2	3	4	5	6	7	8	9	10
Variance (per cent)	81.15	7.47	4.88	2.33	1.50	1.06	0.56	0.41	0.33	0.27
H^{13}CN	0.33	0.15	−0.12	−0.07	−0.04	0.18	0.27	−0.84	0.08	0.10
H^{13}CO$^+$	0.29	0.19	−0.46	−0.74	0.07	−0.07	0.04	0.26	−0.02	−0.10
CCH	0.28	−0.41	−0.47	0.37	0.49	−0.31	−0.09	−0.03	0.16	−0.04
SiO	0.30	−0.12	0.60	−0.17	0.47	−0.15	0.26	−0.01	−0.34	−0.24
HCN	0.32	−0.33	0.18	−0.03	−0.31	−0.03	0.46	0.29	0.49	0.29
HCO$^+$	0.32	−0.28	−0.06	0.04	−0.55	−0.30	−0.19	−0.06	−0.59	0.09
CH$_3$OH	0.26	0.69	0.02	0.38	−0.13	−0.44	0.14	0.14	0.08	−0.17
HC$_3$N	0.33	0.19	−0.11	0.28	0.19	0.58	0.06	0.31	−0.34	0.39
CS	0.33	−0.12	0.04	0.12	−0.22	0.45	−0.22	0.05	0.17	−0.71
SO	0.33	0.12	0.33	−0.14	0.10	−0.06	−0.71	−0.05	0.30	0.34

Note. Correlation coefficient values above 0.8 are highlighted in boldface.

exceeding 80 per cent indicates a strong correlation between components, while a coefficient surpassing 90 per cent signifies a very strong correlation between the components. H^{13}CN, and HC$_3$N, and HCN, HCO$^+$, and CS are strongly correlated, with a correlation coefficient of above 0.93. SiO and SO are highly correlated with

a coefficient of 0.99, suggesting both lines trace similar physical conditions such as outflows and shocks in the protocluster region.

In Fig. 5, we show the distribution of eigenvalues with respect to the PCs. The plot shows a steep decline in eigenvalues. In our analysis, we identify two PCs with eigenvalues greater than 0.5.
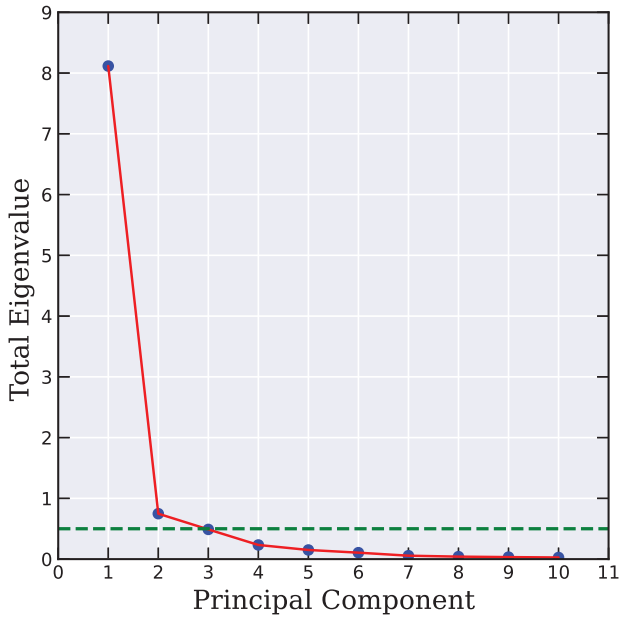
Figure 5. The plot shows the derived eigenvalues of PCs. A threshold eigenvalue of 0.5 is marked with the dashed line.

These two PCs contain the maximum information of the data sets, with a total contribution of about 90 per cent of the total variance. PC1 and PC2 have eigenvalues of 81.15 and 7.47 per cent. We also present the PC3, whose eigenvalue is 4.88 per cent, which is very close to 5 per cent. Fig. 6 shows the variation between pairs of PCs and the contributions of different molecules to these PCs. Fig. 6(a) is between PC1 and PC2, and Fig. 6(b) between PC2 and PC3. We can broadly segregate the molecules into three groups by looking at Fig. 6(a). To get a better insight into their nature, we present the constructed PC maps (PC1, PC2, and PC3) in Fig. 7.

In PCA, PC1 represents the direction of maximum variance in the data set, indicating that it captures the most significant variability among the molecules. As a result, delineating differences among molecules solely based on PC1 can be challenging. However, by examining the contributions of molecules along PC2 and PC3, which represent orthogonal directions capturing additional variance, it becomes feasible to discern distinctions among the molecules more effectively. On PC2, the cyan contours indicate HCN, HCO^+, CCH, SiO, and CS. The lines CCH, HCN, and HCO^+ are highly anticorrelated with PC2. These molecules are more likely to trace gas from the surrounding region of the central massive dense core. The green contours indicate CH_3OH, which is strongly correlated to PC2. This is primarily tracing the dense gas from the central core. $H^{13}CO^+$, $H^{13}CN$, HC_3N, and SO are positively correlated to PC2 because they trace same emission around the central massive core. Similarly, SiO and CS are negatively correlated to PC2, suggesting these might trace some outflow emission in the protocluster. On PC3 (Fig. 7c) map, the cyan contours represent CCH and $H^{13}CO^+$. These molecules appear to be highly anticorrelated to SiO and SO, which are shown in green contours. This anticorrelation could be because CCH and $H^{13}CO^+$ trace some emission around the central core, whereas SiO and SO trace the shock and outflows in the protocluster complex. SO appears to be better correlated to $H^{13}CO^+$, $H^{13}CN$, HC_3N in PC2, since this

molecule can also trace dense gas, and the spatial distribution (see Fig. 4) supports the similarity. HCN and CS are slightly correlated with PC3, which means these lines also trace some outflow emission.

Considering the PC1 versus PC2 plot (Fig. 6a), we broadly segregate the molecules into three groups. First group contains $H^{13}CN$, $H^{13}CO^+$, HC_3N, and SO, and the second group contains HCN, HCO^+, CCH, SiO, and CS. The third group is the CH_3OH. Note that this classification is not strict since the molecules might trace multiple physical conditions. This is visible on the PC2 versus PC3 plot (Fig. 6b), where the correlation between molecules appears slightly different. This analysis provides an opportunity to segregate the molecules into different groups, which trace emissions of different physical conditions in the protocluster complex IRAS 15394−5358. In a similar analysis towards G9.62+019, Liu et al. (2020) see a slightly different grouping of molecules, suggesting differences in the nature of the surrounding environment in different star-forming regions. More studies of the ATOMS survey will help get a deeper insight into the molecular line emissions by characterizing the gas distributions.

3.2.3 Hub-filament system

Within the massive clump of 15394−5358, we can see the presence of a hub-filament system. The growing observational evidences indicates these hub-filament systems are the preferable sites of massive star formation, where matter from the surroundings gets funnelled to the central core or hub through the filaments. We can detect the filamentary structures in the star-forming clump using the $H^{13}CO^+$ line transition. The reason for using this transition in filament identification is the following. The high critical density (6.2×10^4 cm^{-3} at 10 K) and low optical depth make the $H^{13}CO^+$ J $= 1 - 0$ transition a good tracer of dense gas. Effective excitation density (3.9×10^4 cm^{-3}; Shirley 2015) of the molecule is comparable to its critical density. Also, the $H^{13}CO^+$ J $= 1 - 0$ line emission correlates well with the dense gas column density traced by *Herschel* data (Shimajiri et al. 2017; Li et al. 2022). Due to this property, Zhou et al. (2022) used this line to identify the filaments toward the targets of the ATOMS survey. Applying the FILFINDER algorithm (Koch & Rosolowsky 2015) over the moment0 maps of $H^{13}CO^+$ J $= 1 - 0$, these authors have identified the filaments associated with all the targets.

Zhou et al. (2022) identified four major filamentary structures extending from the central hub (C-1), creating the hub-filament system in the protocluster complex 15394−5358. In this work, we use the same filaments identified by Zhou et al. (2022). Fig. 8 presents the identified hub-filament system. The filaments (F1 to F4) are the yellow lines. In a next section, we discuss the nature of infall onto the central core through the filaments.

3.2.4 Gas kinematics

In this section, we discuss the kinematics of the central hub of the protocluster complex. To obtain the kinematics of the hub, we extract the spectra over the core C-1. This will provide a global kinematic property of the central part of the protocluster region. In Fig. 9, we show the average spectra of the ten molecular line transitions. Spectra of $H^{13}CO^+$, CH_3OH, HC_3N, CCH, SiO, CS, and SO show single profiles. Extended line wings are seen especially in SiO, CS, and SO is a signature of outflows. The multiple peaks in $H^{13}CN$ and HCN are due to their hyperfine nature.
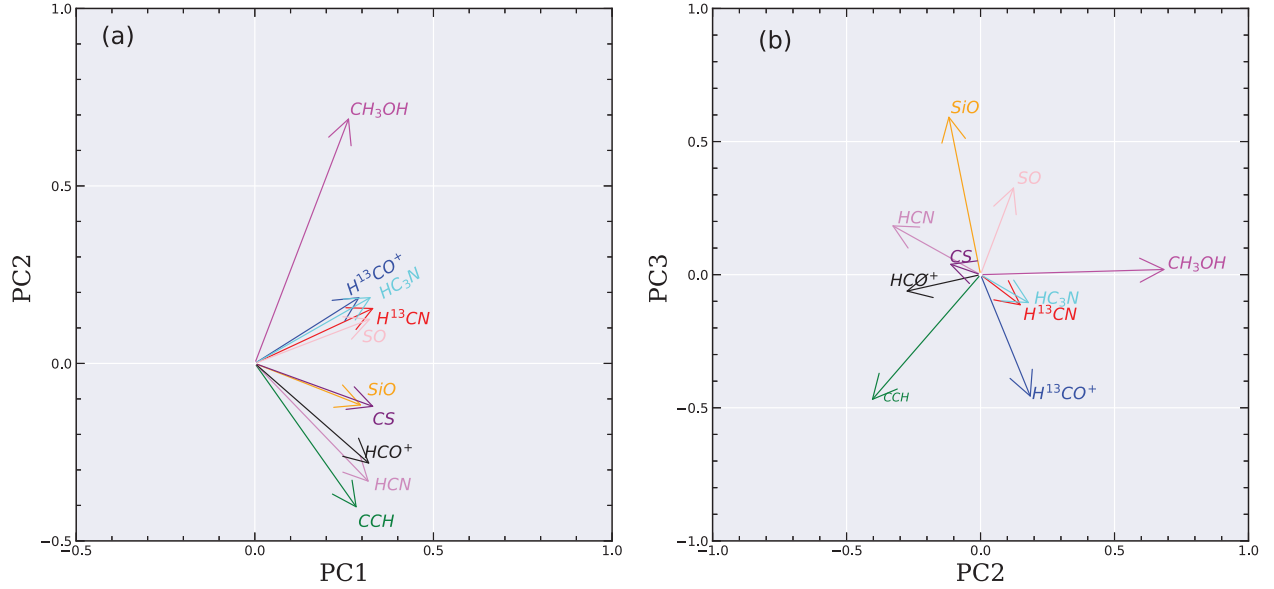
Figure 6. The plots show variations between PC1 and PC2 (a) and between PC2 and PC3 (b). Contributions from each molecule to the PCs are represented as arrows.
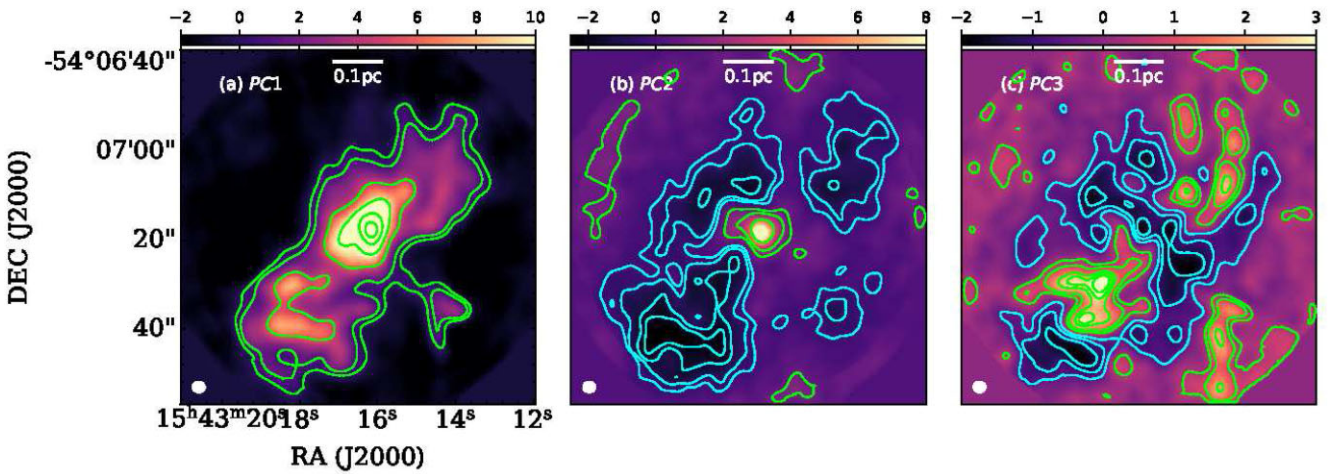

Figure 7. Maps of the generated first three PCs. (a) PC1 is overlaid with its contours at levels of 0, 1, 5, 10, 15, and 20. (b) PC2 has contour levels of -2.0, -1.5, -0.7, -0.3, 1, 2, and 5. (c) PC3 has contour levels of -1.5, -1.0, -0.5, 0.5, 1, 1.5, 2, 2.5, and 3. The maps show contours with negative and positive values in cyan and green colours, respectively. The different components, especially PC2 and PC3 demarcates the distinctions among the different molecules.

3.2.5 Molecular outflows

Towards the protocluster, we conducted a search for outflows in the SiO, CS, and SO lines. The blue and redshifted gas in these lines were integrated within the velocity ranges of [-56.25, -44.87] and [-37.92, -27.17] km s^{-1} for SiO, [-49.24, -43.27] and [-37.29, -28.33] km s^{-1} for CS, and [-45.57, -42.62] and [-38.20, -33.77] km s^{-1} for SO. The outflow lobes identified from these lines are illustrated in Fig. 10.

The outflow emissions appear extended and exhibit similar morphology for the SiO and CS lines, whereas the outflow is more compact in SO. It is plausible that the low-level extended emission of SO lies below the sensitivity level of the observations. The outflows extend diagonally in the northwest and southeast directions emanating from the central massive core, with the blueshifted gas extending in the southeast direction and the red-

shifted gas extending in the northwest direction. The detection of outflows from the central core indicates underlying star formation activity.

3.2.6 Velocity gradient and activity within central hub

Fig. 11 presents the H^{13}CO$^+$ moment1 and moment2 images of IRAS 15394−5358. The moment1 map is displayed in Fig. 11(a). From this map, we can see a gradual gradient in velocity along the filamentary structures. The gradient is blueshifted on the hub's eastern side and redshifted on its western side. The filaments F1 and F4 are located along the blueshifted gas, whereas the filaments F2 and F3 lie on the redshifted gas. So, essentially, the gas is transferred to the hub from its surroundings. We discuss the nature of the velocity gradients along the filaments in Section 5.
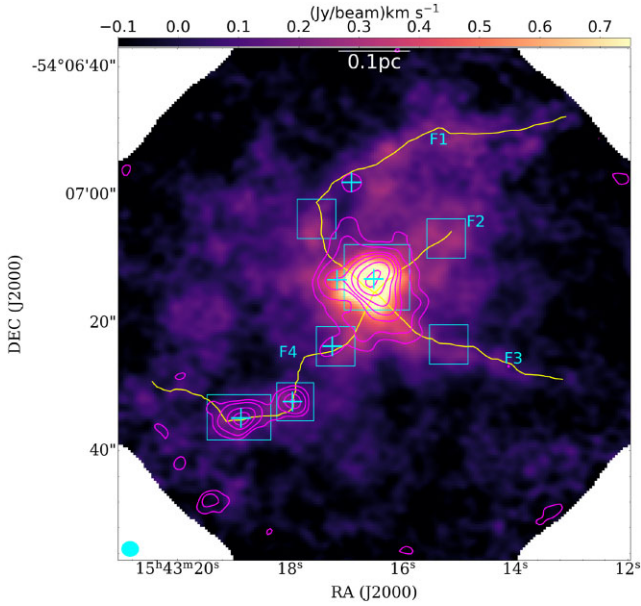
Figure 8. Integrated intensity map of $H^{13}CO^+$. The filaments are shown as yellow lines and labelled from F1 to F4. The 3 mm continuum emission is shown as magenta contours, with the same contour levels as of Fig. 2. The ' + ' marks display the locations of the identified dense cores in the region. The cyan boxes on the central core and the filaments are the regions where spectra are extracted to analyse the infall signature in that region.

Fig. 11(b) illustrates the moment2 map. This map exhibits a higher value (~ 1.8 km s^{-1}) in the hub compared to its surrounding region. The other prominent cores, C-2 and C-3, do not show significantly enhanced linewidths. The increased linewidth of the central core reflects underlying feedback-driven activity. It could also indicate core rotation, not resolved by the current observations. The primary reason behind the enhanced linewidth is likely the energetic outflows and stellar winds from the massive protostars. Additionally, inflows dominated by gravity or turbulence towards the hub could contribute to the higher linewidth values.

The $H_{40\alpha}$ line does not exhibit any emission towards the protocluster. We also searched for radio emission towards the region from surveys such as the 843 MHz SUMSS (Sydney University Molonglo Sky Survey; Mauch et al. 2003) and 21 cm continuum SGPS (The Southern Galactic Plane Survey; McClure-Griffiths et al. 2005) and found no emission towards the protocluster. Previous studies also reported non-detection of radio emission towards IRAS 15394−5358 (Garay et al. 2006). Also, no luminous young stellar object (YSO) or UC H II region has been detected from these surveys or previous studies towards the region (Liu et al. 2021; Zhang et al. 2023).

The core C-1 is associated with massive star formation and is at an early stage of evolution, as evidenced by the presence of a 6 GHz CH_3OH maser (Caswell 1998) and EGOs (Cyganowski et al. 2008). It is likely that the dynamical motion of the inflows driven by gravity/turbulence, along with outflows and stellar winds, are playing a significant role in the enhanced linewidth. The map displays a few pixels with higher values (near filament F2). These higher values appear as red spots in the linewidth map, which might be due to local gas distributions but could also be artefacts.

3.2.7 Velocity-integrated channel and position-velocity maps

For a deeper understanding of the kinematics of the hub-filament system, we generated velocity-integrated channel and position-velocity (PV) maps using the $H^{13}CO^+$ line. In Fig. 12, we present the channel maps generated by integrating the line in steps of 1 km s^{-1}, starting from −46 to −34 km s^{-1}. The channel maps provide a detailed view of the kinematic properties of the hub-filament system. Each panel displays the emission within a specific velocity range, capturing the dynamic motions of gas within the system. As the velocity increases from −46 to −34 km s^{-1}, we observe distinct shifts in the intensity and spatial distribution of the emission.

At higher velocities (e.g. −46 to −44 km s^{-1}), the intensity is predominantly associated with filament F4, which may imply active gas flows along this structure. Between velocities −44 and −42 km s^{-1}, the emission becomes more prominent around filament F1 as well as F4. The emission is dominated by filament F1 within the velocity range of −42 to −41 km s^{-1}. The velocity range of −41 to −39 km s^{-1} shows significant emission from filaments F2 and F3. In the lower velocity ranges (e.g. −39 to −34 km s^{-1}), the intensity around filaments F2 and F3 starts to fade, and the emission appears as a red spot towards the centre. The significant red regions on the maps highlight areas of higher gas density, many of which are associated with the identified dense cores of the protocluster. These channel maps suggest that the filaments in the protocluster are crucial conduits for channelling gas into the central region and the dense cores, especially filaments F1 and F4. The dense cores, marked by plus signs, are consistently located along these filaments, indicating that they are focal points for gas accumulation and potential star formation.

This kinematic structure illustrates how gas is funnelled along the filaments towards the dense cores, supporting the ongoing star formation processes in the hub-filament system. The observed velocity gradients further corroborate the information regarding velocity gradients seen in the $H^{13}CO^+$ moment1 map shown in Fig. 11(a), where filaments F1 and F4 appear blueshifted, and filaments F2 and F3 are redshifted with respect to the central hub. This scenario is depicted in Fig. 18 and discussed in Section 5.1.

To further explore the velocity gradient and the funnelling of gas towards the central hub, we generated the PV-map along the white horizontal line shown in Fig. 12, compressing it over the entire declination range. The PV-map, shown in Fig. 13, provides complete velocity information across the protocluster, spanning the full right ascension range. The PV-map reveals a typical V-shaped structure, usually attributed to strong velocity streams converging towards the central location (Tokuda et al. 2019; Neelamkodan et al. 2021; Arzoumanian et al. 2022). This V-shaped structure indicates a velocity gradient from both the eastern and western sides towards the central hub. The velocity gradients on the eastern and western sides predominantly correspond to the velocity structures of filaments F4 and F1, respectively. Although filaments F2 and F3, located on the western side of the hub, also show velocity gradients, their gradients are shallower compared to filament F1. The presence of this gradient feature in the protocluster is further discussed in Section 5.1 and illustrated in Figs 17 and 18.

We fitted the two velocity streams and found that the eastern side has a higher gradient of 24.41 ± 1.11 km s^{-1}pc^{-1}, while the western side has a lower gradient of 13.95 ± 1.13 km s^{-1}pc^{-1}. This is nearly half the gradient observed on the eastern side of the hub. This may imply that the eastern side is more active in funnelling mass to the hub, due to filament F4. This observation is also supported by
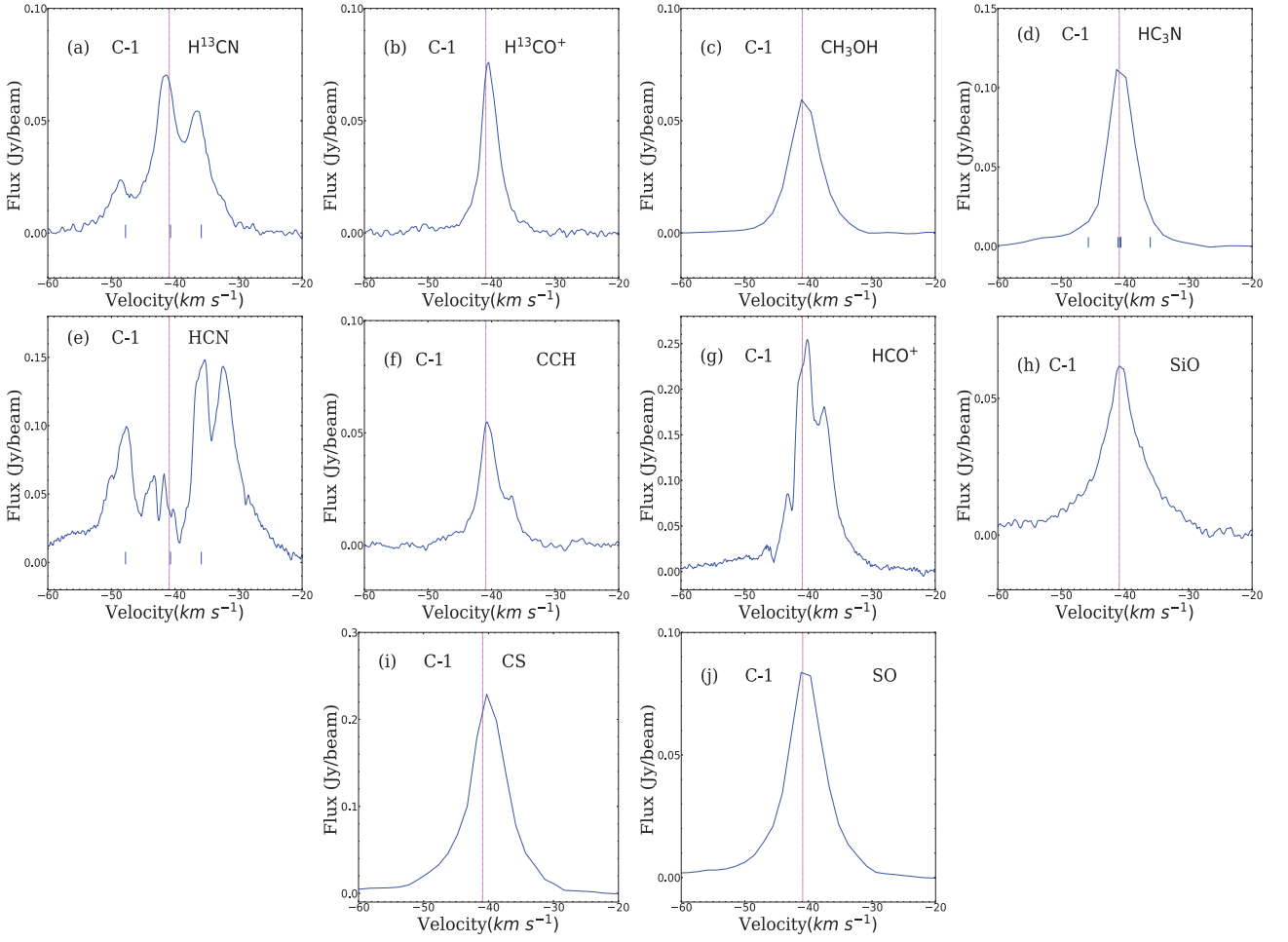
Figure 9. Average spectra of all the molecular lines extracted over the central core C-1. The vertical straight line in each panel marks the LSR velocity of -40.9 km s^{-1} obtained from CS(2 − 1) molecular line transition (Bronfman et al. 1996). The small vertical blue lines on plots of H^{13}CN, HC$_3$N, and HCN mark the positions of hyperfine components in those line transitions.
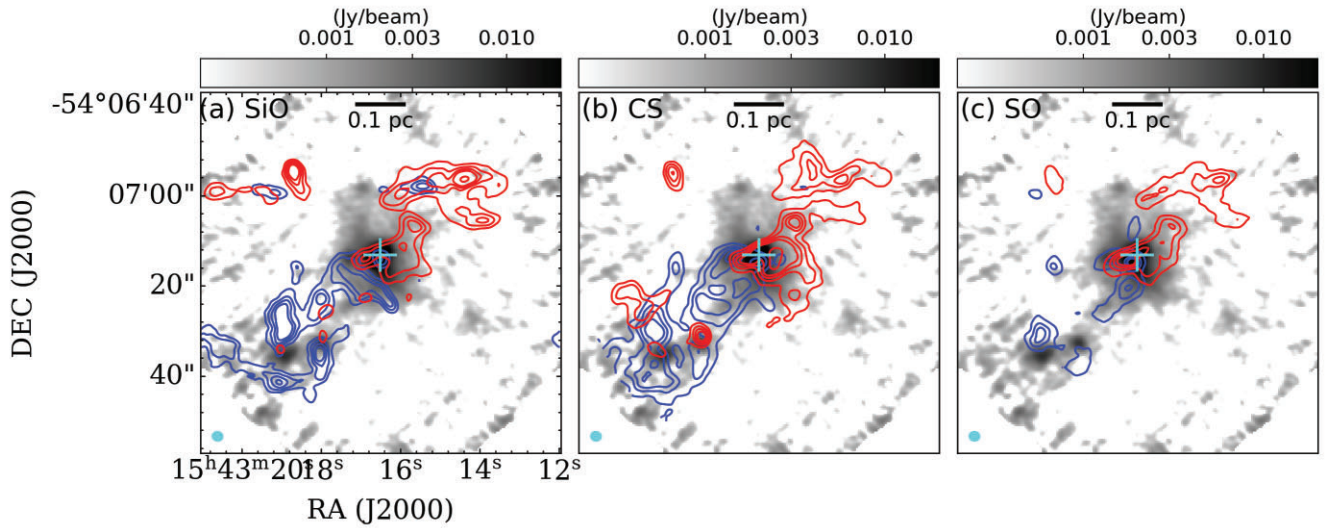
Figure 10. The background greyscale represents the 3 mm dust continuum map, on top of which outflows from SiO (a), CS (b), and SO (c) are overlaid. The contour levels are set at 3, 5, 7, 9, 15, and 20 times σ, where $\sigma = 0.07, 0.17,$ and 0.1 (Jy beam^{-1}) km s^{-1} for SiO, CS, and SO, respectively. The ' + ' mark indicates the location of the central core C-1A.
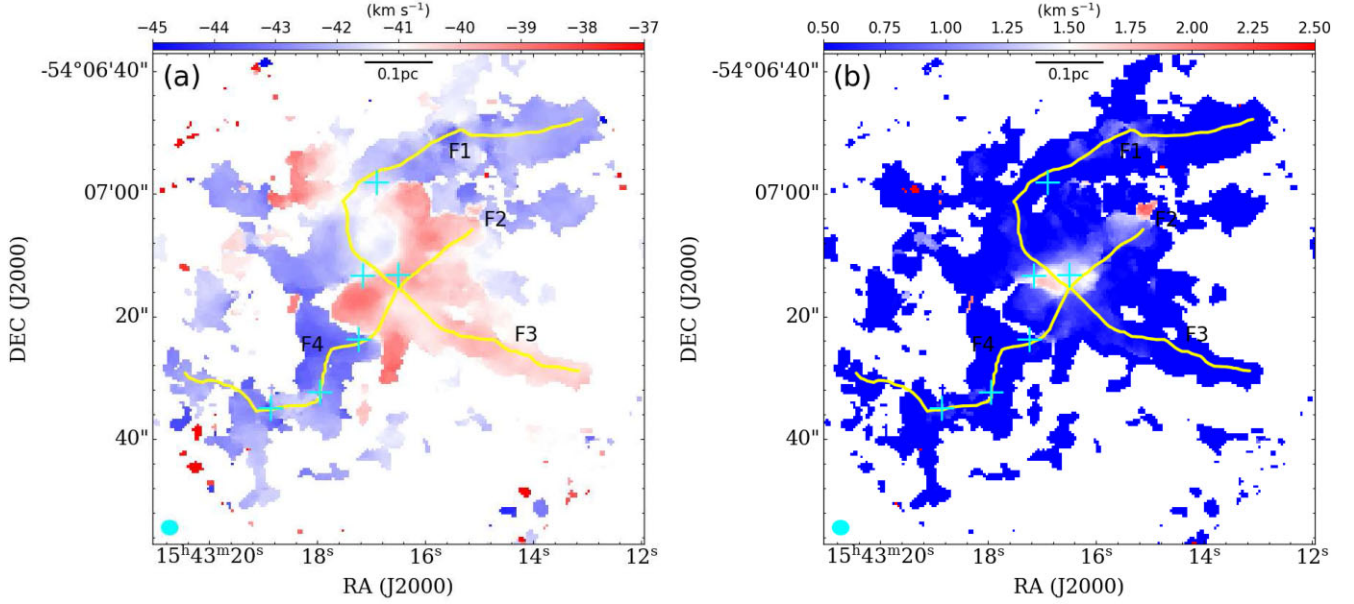
Figure 11. Moment1 (a) and moment2 (b) maps of $H^{13}CO^+$ line transition. Filaments, along with their labels, are overplotted on the maps. The ' + ' marks are the locations of the dense cores. Both the moment maps are generated within velocity range of [-48.1, -29.7] km s^{-1} and considering pixels above 5σ, where $\sigma = 0.009$ Jy beam^{-1}. Scale bar and beam size are also shown on the maps.

the discussions in Section 5.1 and Fig. 18, where it is evident that filament F4 is relatively more blueshifted and may be more active in channelling gas to the hub compared to the other filaments. The mean velocity gradient towards the hub is ~ 20 km s^{-1}pc^{-1}, facilitating the channelling of gas through the filaments towards the hub, thereby increasing its mass and aiding in the formation of massive star(s) within the hub.

Given the significant mean velocity gradient observed, it can be interpreted as indicative of a globally collapsing scenario in this massive star-forming clump. The velocity gradient observed towards IRAS 15394−5358 is comparable to those observed on small scales in massive star-forming regions (Zhou et al. 2022; Hacar et al. 2023; Xu et al. 2023; Mai et al. 2024) and in simulation studies (Smith et al. 2020). At such small scales (< 1 pc), the velocity gradient could primarily be gravity-driven (Zhou et al. 2022), leading to mass inflows and variations in density structures due to local conditions. This velocity gradient in the protocluster clearly indicates a globally collapsing scenario, where mass inflow through the filaments is evident (e.g. Peretto et al. 2013). In such a scenario, the gravity-driven inflows within clumps might become more complex and chaotic, with evolution leading to the mass growth of the associated cores (Rigby et al. 2024). However, on a larger scale (> 1 pc), the velocity gradient could be much smaller (< 5 km s^{-1}pc^{-1}), showing signatures of global collapse (Zhou et al. 2022, 2023; Seshadri et al. 2024).

4 STAR FORMATION PROPERTIES OF THE PROTOCLUSTER REGION

4.1 Virial analysis of cores

We carry out the virial analysis to asses the gravitational stability and kinematics of the cores. We calculated the virial parameter using the expression (Bertoldi & McKee 1992):

$$\alpha_{\rm vir} = \frac{5\sigma_v^2 R_{\rm core}}{G M_{\rm core}}, \tag{2}$$

where G is the gravitational constant, σ_v is the velocity dispersion, $R_{\rm core}$, and $M_{\rm core}$ are the radius and mass of the core, respectively. The above equation neglects the effect of magnetic field. The velocity dispersion is expressed as $\sigma_v = \Delta V/\sqrt{8\ln2}$, where ΔV is the full width half maximum (FWHM) velocity width. To estimate this parameter, we use the $H^{13}CO^+$ (1−0) line, which can be optically thin in nature. The FWHM velocity width of the cores is obtained by fitting their $H^{13}CO^+$ spectra. The derived value of $\alpha_{\rm vir}$ for all the cores are listed in the last column of Table 1.

For a core to undergo gravitational collapse, it needs to be subvirial, for which $\alpha_{\rm vir} \leqslant 2$. In contrast, if the core is supported against the gravitational collapse, it must be supervirial. Such cores must expand or might stay confined under the effect of external pressure or magnetic force (Kauffmann, Pillai & Goldsmith 2013). For all cores, the value of $\alpha_{\rm vir}$ lies in the range of $0.01 - 0.94$. This indicates that all the cores are subvirial and gravitationally bound. These cores are expected to collapse leading to the formation of stars.

4.2 Fragmentation

The ALMA 3 mm continuum image reveals the presence of multiple cores within the single ATLASGAL clump. If the fragmentation is happening by the criteria of thermal Jeans instabilities, then the homogenous self-gravitating clump will break into smaller objects defined by the Jeans length (λ_J) and Jeans mass (M_J). These are given by (e.g. Wang et al. 2014; Palau et al. 2015; Sanhueza et al. 2017, 2019).

$$\lambda_{\rm J} = \sigma_{\rm th}\left(\frac{\pi}{G\rho}\right)^{1/2} \text{ and } M_{\rm J} = \frac{\pi^{5/2}}{6}\frac{\sigma_{\rm th}^3}{\sqrt{G^3\rho}}, \tag{3}$$

where ρ is the volume density of the clump derived using the mass and radius values from Urquhart et al. (2018), and $\sigma_{\rm th}$ is the thermal velocity dispersion given by

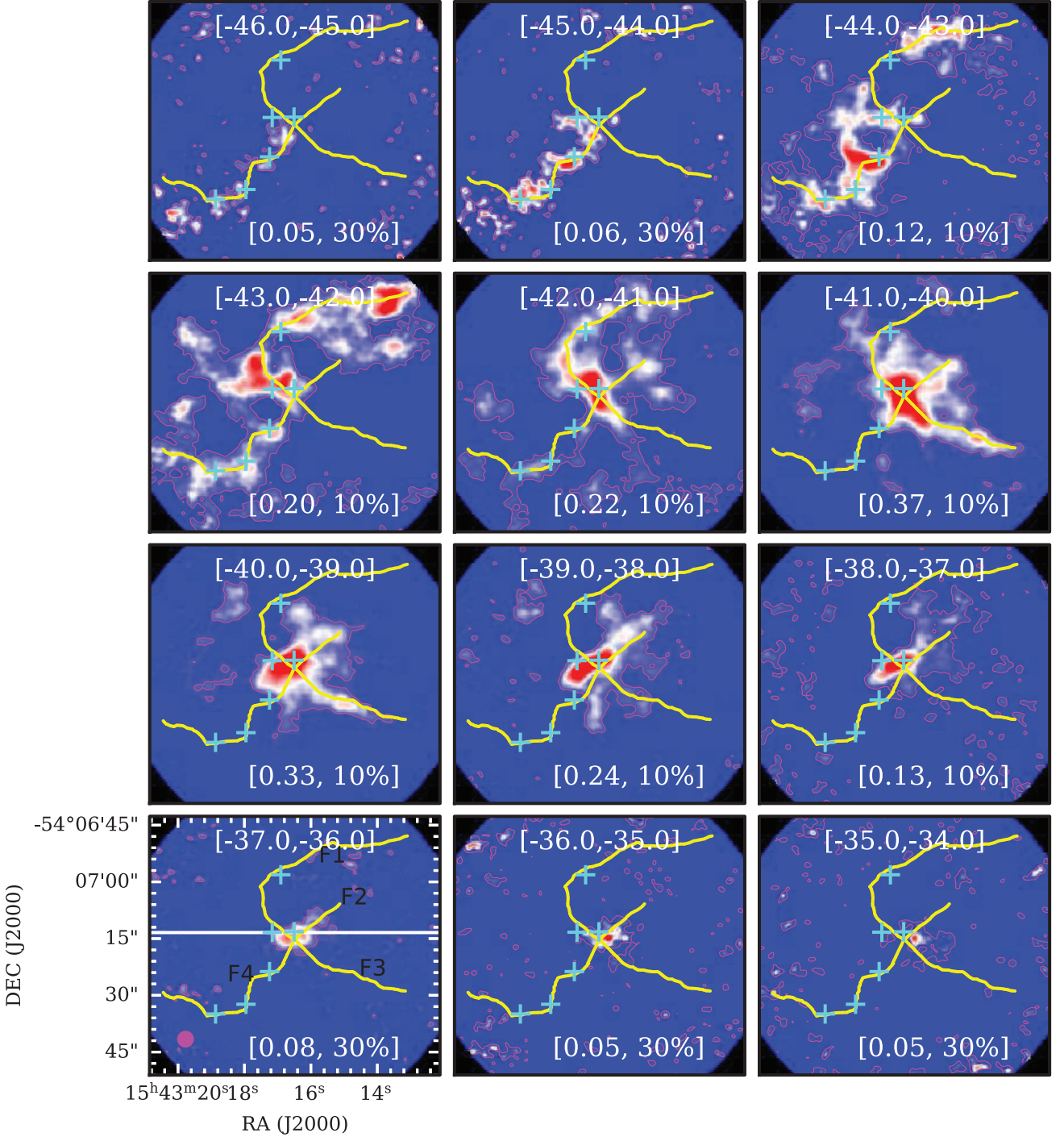$$\sigma_{\rm th} = \left(\frac{k_B T_{\rm kin}}{\mu m_H}\right)^{1/2}, \tag{4}$$

Figure 12. Channel maps of $H^{13}CO^+$ are presented. Each panel displays the velocity-integrated intensity within a velocity range of 1 km s^{-1}. The numbers in square brackets at the top of each panel indicate the velocity range, while the numbers in square brackets at the bottom right of each panel represent the peak value of the map and the percentage of the peak value shown as contour. The locations of the dense cores and filaments are marked in all panels, as in Fig. 11. The beam size of the map is shown in the bottom left corner of the bottom left panel. The PV map, generated along the white straight line shown in the bottom left panel, compressed over the full declination range and is presented in Fig. 13.

where k$_B$, T_{kin}, μ, and m$_H$ are Boltzmann's constant, kinetic temperature, mean molecular weight, and the mass of hydrogen atom, respectively. We assume the clump's kinetic temperature is the same as the dust temperature of 20 K and $\mu = 2.37$ (Kauffmann et al. 2008; Potdar et al. 2022). Importing other parameters into the above

equations, we obtain the thermal Jeans length and Jeans mass to be 0.16 pc and 4.4 M$_\odot$, respectively.

It is also essential to consider the non-thermal contribution arising from turbulence in the calculations. To take into account the non-thermal contribution, the thermal velocity dispersion needs to be
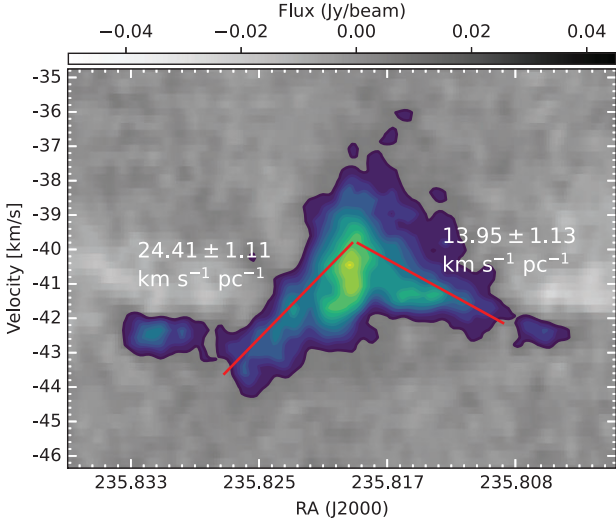
Figure 13. The position–velocity diagram of $H^{13}CO^+$ is extracted along the white horizontal line shown in Fig. 12 (at DEC = −54 : 07 : 13.80) and compressed over the entire declination range. The coloured filled contours range from 10 per cent to 90 per cent of the peak value (0.045 Jy beam^{-1}) in steps of 10 per cent. The red lines represent the fitted velocity gradients from both the eastern and western sides of the central hub.

Table 3. Density of clump and derived Jeans parameters.

ρ	$\lambda_{\mathrm{Jeans}}^{\mathrm{Th}}$	$M_{\mathrm{Jeans}}^{\mathrm{Th}}$	$\lambda_{\mathrm{Jeans}}^{\mathrm{Turb}}$	$M_{\mathrm{Jeans}}^{\mathrm{Turb}}$
(g cm^{-3})	(pc)	(M$_\odot$)	(pc)	(M$_\odot$)
1.4×10^{-19}	0.16	4.4	0.30	28.0

replaced with total velocity dispersion as follows (Wang et al. 2014; Liu et al. 2019; Li et al. 2023)

$$\sigma_{\mathrm{tot}} = \left(\sigma_{\mathrm{nt}}^2 + \sigma_{\mathrm{th}}^2 \right)^{1/2}, \tag{5}$$

where the non-thermal velocity dispersion can be derived from the observed lines using the following expression

$$\sigma_{\mathrm{nt}} = \sqrt{ \sigma_{\mathrm{line}}^2 - \frac{k_B T_{\mathrm{kin}}}{m_{\mathrm{line}}} }, \tag{6}$$

where σ_{line} is the velocity dispersions observed from the molecular line transition, m_{line} is the molecular mass of the molecule. We use the optically thin $H^{13}CO^+$ line to obtain the velocity dispersion σ_{line}. We determine the velocity dispersion from spectra obtained from a region away from the cores. This is to ensure that the measured velocity dispersion is not affected by the current star formation activity of the complex. We derive the turbulent Jeans length and mass as 0.30 pc and 28 M$_\odot$, respectively. Table 3 gives all the derived Jeans parameters.

4.3 Thermal versus turbulent Jeans fragmentation

In this section, we try to understand the dominant mechanism responsible for the fragmentation of the clump into several cores. For this purpose, it is necessary to compare the core separation and masses. Here we apply the minimum spanning tree (MST) method to derive the core separation. Using MST, we can generate a set of straight lines connecting a set of points or nodes. This algorithm generates the straight lines so that the sum of lengths of all straight
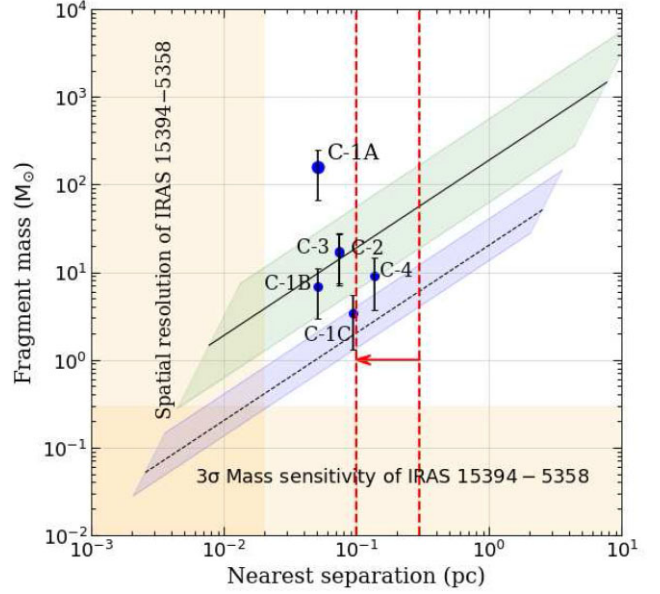

Figure 14. Fragment mass versus the nearest separation. Here, the fragment masses are the core masses. The blue-filled circles represent the associated cores of IRAS 15394−5358. The dotted, solid black line and the shaded regions are plotted following the outlines described in Wang et al. (2014) and Xu et al. (2023). Spatial and 3σ mass sensitivity of IRAS 15394−5358 with ALMA Band-3 observations is shown as an orange-shaded region. The 3σ mass sensitivity estimated using the 3σ flux density and dust temperature of 100 K. The black dotted line is for thermal Jeans fragmentation with $T = 15$ K and density $n = [10^2, \, 10^8 \ \mathrm{cm}^{-3}]$. The blue-shaded region corresponds to the same density range, but for temperatures, $T = [10, 30]$ K. The solid black line is for the turbulent Jeans fragmentation corresponding to velocity dispersion $\sigma = 0.7 \ \mathrm{km \, s^{-1}}$ and density $n = [10^2, \, 10^8 \ \mathrm{cm}^{-3}]$. The green shaded region is for the same density but with velocity dispersion $\sigma = [0.4, 1.2] \ \mathrm{km \, s^{-1}}$. All cores are labelled on the plot. Due to their similar masses, cores C-2 and C-3 overlap with each other. The red vertical dashed lines mark the location of 0.3 pc ($\lambda_{\mathrm{Jeans}}^{\mathrm{Turb}}$ or Jeans length assuming the cloud fragmented when its density was $10^4 \ \mathrm{cm}^{-3}$) and 0.1 pc, the median value of the observed core separation, respectively. The red arrow shows the length of 0.2 pc, highlighting the difference.

lines is minimum. In our analysis, the nodes are the locations of cores, and the straight lines connecting the nodes provide spatial separation between the cores. Due to the projection effect, the derived separation between the cores is smaller than the actual separation by a factor of $(2/\pi)$ (Sanhueza et al. 2019; Saha et al. 2022). We derive the core separations in the range of $0.03 − 0.14$ pc with a median value of 0.07 pc. For cores, the mass lies in the range of $3.4 − 157$ M$_\odot$ with the median value of 13 M$_\odot$.

In our case $\lambda_{\mathrm{obs}} < \lambda_{\mathrm{Jeans}}^{\mathrm{Th}} < \lambda_{\mathrm{Jeans}}^{\mathrm{Turb}}$ and $M_{\mathrm{Jeans}}^{\mathrm{Th}} < M_{\mathrm{obs}} < M_{\mathrm{Jeans}}^{\mathrm{Turb}}$. To compare the thermal and turbulent Jeans fragmentation, Wang et al. (2014) have analysed the core mass distribution with core separation. The same procedure has also been used by Xu et al. (2023) and Morii et al. (2024). In this work, we follow the same procedure to compare the thermal and turbulent Jeans fragmentation mechanism. In Fig. 14, we show the mass separation distribution for all six cores in this work. The straight black lines (dotted and solid) and the shaded region are plotted following discussions of Wang et al. (2014) and Xu et al. (2023). The caption of the figure has the details of the lines and shaded regions.

The observed core separation matches the thermal Jeans length, whereas the thermal Jeans mass is significantly less than the observed

median value. However, it is close to the lowest mass among all cores. In Fig. 14, C-1A lies above the green shaded region, whereas cores C-2 and C-3 lie within it. Among the other three cores, C-1C is within the blue shaded region, C-4 is very close, and C-1B is nearer when considering its error. However, caution should be taken when interpreting the mechanism responsible for fragmentation. The recent work by Vázquez-Semadeni et al. (2024) suggests that turbulence might not be an effective mechanism to counteract gravity, and to understand the fragmentation mechanism, it is essential to compare the separation between the cores rather than the mass of the cores.

In the protocluster, the observed median separation between the cores is approximately 0.1 pc, whereas it is 0.3 pc as derived from turbulent Jeans fragmentation (see Fig. 14). Assuming that fragmentation took place when the cloud was 10^4 cm^{-3} and at 20 K, this yields a Jeans length of approximately 0.3 pc. It is possible that fragmentation occurred at an earlier stage of evolution. To understand this delay, we refer to the discussions in Xu et al. (2024), which explain that the core separation would tighten over time by a length (Δl), which is expressed as follows:

$$\Delta l = 0.088 \times \left(\frac{R_{cl}}{1\,pc} \right) \left(\frac{n_{H_2}}{10^4\,cm^{-3}} \right)^{0.5} \left(\frac{t_{life}}{5 \times 10^4\,yr} \right) \; pc, \quad (7)$$

where R_{cl} is the clump radius (Urquhart et al. 2018), and $n_{H_2} = \rho/\mu_{H_2} m_H$ is the number density of the clump, estimated to be 3×10^4 cm^{-3}. Using these values, we derive the value of time, t_{life}, over which the cores will tighten by 0.2 pc, to be 1.3×10^5 yr. This is in agreement with the typical statistical lifetime of massive starless clumps (Motte et al. 2018).

This suggests that in the protocluster, the fragmentation occurred at an earlier evolutionary stage dominated by the thermal Jeans fragmentation mechanism. At a later stage, due to collapse, the cores grew in mass through accretion and became closer, as observed by Xu et al. (2024). The growth in mass of cores C-2 and C-3 is due to filament F4, which is the major contributor of gas inflow with a higher velocity gradient. However, the extremely high mass of C-1A compared to its neighbours might have resulted from mass accumulation due to the inflow of gas through the filaments, whereas the mass of the other cores may be primarily due to fragmentation alone (Li, Cao & Qiu 2021). Hence, the discrepancies observed between the observed and the thermal Jeans parameters can be attributed to the delay between the time of fragmentation, when the density was lower, and the time of observation.

In the SDC335 star-forming region, it was mentioned that turbulence dominates the fragmentation of clumps into cores and cores into condensations (Xu et al. 2023). Some earlier studies have also observed similar results, where turbulence pressure seems to dominate over thermal pressure for hierarchical fragmentation in protocluster regions (Wang et al. 2014; Rebolledo et al. 2020; Xu et al. 2023). Contrary to this, fragmentation driven by thermal pressure in protoclusters has also been observed in several studies (Palau et al. 2015; Potdar et al. 2022; Saha et al. 2022).

In a systematic study of a series of protoclusters, Xu et al. (2024) have found that massive protoclusters are in a totally dynamic state, where the cores will keep accreting mass. This will make the observed core mass much larger than expected from the static Jeans fragmentation (Li 2024). So another possibility is that the core is small in mass and keeps accreting mass until it reaches a mass comparable to the turbulent Jeans fragmentation. Therefore, caution must be taken when interpreting super-Jeans masses as being due to
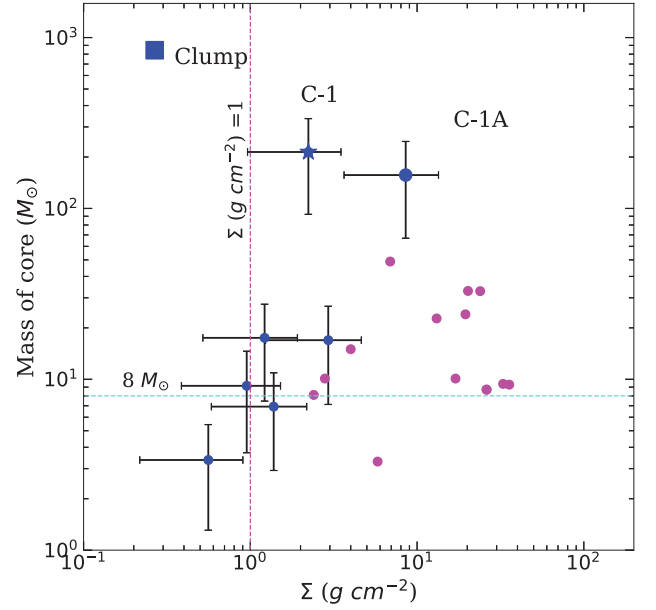

Figure 15. Surface density versus core mass. The blue-filled circles are the cores associated with IRAS 15394−5358, and the magenta-filled circles are from Saha et al. (2022). The blue-filled star and square represent the hub C-1 and the whole clump, respectively. The vertical and the horizontal lines are for surface density of 1 g cm^{-2}, and core mass of 8 M$_\odot$, respectively.

turbulent support, as they may correspond to thermal fragmentation within a globally collapsing clump.

In Fig. 14, core C-1A stands out from the rest of the cores due to its higher mass compared to all other cores. Core C-1B is closest to C-1A, separated by 0.05 pc, just above the spatial resolution of IRAS 15394−5358. It is expected that the central core C-1A might hold further substructures/condensations within itself, similar to SDC335 MM1 (Xu et al. 2023), G335-MM1 (Olguin et al. 2021, 2022). Further high-resolution observations with a spatial resolution of ∼0.01 pc would enable to probe of the fragmentation within the core C-1A.

4.4 Nature of high-mass star formation in the protocluster region

In previous sections, we derived the physical parameters and analysed the virial state of the cores. All the cores are gravitationally bound and prone to form stars. The core C-1A is the most massive with a mass of 157 ± 90 M$_\odot$, with a radius of 0.04 pc and a surface density of 8.9 ± 4.9 g cm^{-2}. In this section, we discuss the star formation properties of the cores.

In Fig. 15, we plot the core masses with respect to their surface density. For comparison, we also plotted the central hub C-1 and the full ATLASGAL clump. We derive the clumps' surface density using the mass and radius values from Urquhart et al. (2018) (see Section 1). The clump's surface density (0.27 g cm^{-2}) is less than 1 g cm^{-2}. However, the surface density of the central hub C-1 is similar to the massive core C-1A. Along with the cores associated with IRAS 15394−5358 (blue-filled circles), we also plot the cores associated with protoclusters G12.42+0.50 and G19.88−0.53 (Saha et al. 2022) from previous ATOMS studies. Among all the cores, C-1A stands out as the most massive. Out of six cores, two cores (C-1C, ad C-4) have $\Sigma < 1$ g cm^{-2}. C-1A is one of the densest and
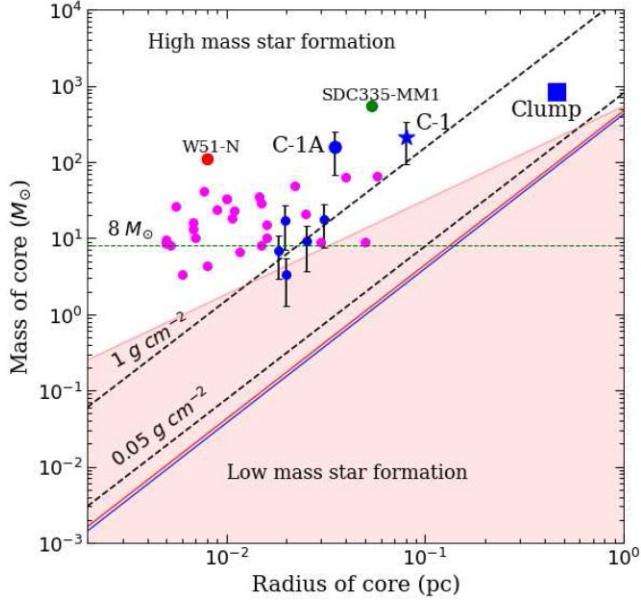
Figure 16. Radius versus mass. The blue-filled circles mark the positions of the cores associated with IRAS 15394−5358. The blue-filled star and square represent the hub C-1 and the whole clump. Cores from literature (Peretto, Hennebelle & André 2007; Zapata et al. 2009; Rathborne et al. 2011; Wang et al. 2011; Peretto et al. 2013; Saha et al. 2022) are also shown in the plot as magenta-filled circles. SDC335-MM1 (Peretto et al. 2013), and W51-N (Zapata et al. 2009) are displayed as green and red-filled circles, respectively. The blue and red lines represent the surface density thresholds of $116 \, M_\odot \, pc^{-2}$ ($\sim 0.024 \, g \, cm^{-2}$) and $129 \, M_\odot \, pc^{-2}$ ($\sim 0.027 \, g \, cm^{-2}$) from Lada, Lombardi & Alves (2010) and Heiderman et al. (2010), respectively. The shaded region is for the low-mass star formation, which does not satisfy the criteria of $m(r) > 870 \, M_\odot \, (r/pc)^{1.33}$ (Kauffmann et al. 2010). Surface density thresholds of $0.05 \, g \, cm^{-2}$ (Krumholz & McKee 2008), and $1 \, g \, cm^{-2}$ (Urquhart et al. 2014) are shown as dashed black lines. The green dashed line is for a core mass of $8 \, M_\odot$.

most compact protostellar cores. To analyse the star formation nature of the cores, we compare the mass of cores with their radius.

In Fig. 16, we present the distribution of core mass relative to their radius, accompanied by the central hub C-1, the entire massive clump, and individual cores, offering insights into their star formation characteristics. Notably, the high-mass star formation properties of both C-1 and the entire clump are discernible from the plot. Additionally, for comparison purposes, cores from the literature are included in this figure. Among cores of similar radius, core C-1A stands out by its significant mass. This core ranks among the most massive protostellar cores in the Galaxy. Its mass is comparable to that of SDC335-MM1 (Peretto et al. 2013) on a larger scale, and on a smaller scale, to the massive cores detected in Cygnus-X (Bontemps et al. 2010).

We compare the massive star formation properties of the core C-1A with already known massive star-forming cores SDC335-MM1 (Peretto et al. 2013) and W51-N (Zapata et al. 2009). SDC335-MM1 has a mass of $\sim 550 \, M_\odot$ within a radius of ~ 0.05 pc. Along with other low-mass objects, this core has the potential of forming a massive star of $\sim 50 - 100 \, M_\odot$. The other massive protostellar core W51-N has a mass of $110 \, M_\odot$. According to Zapata et al. (2009), this core is hosting a massive star of $\sim 65 \, M_\odot$ with an accreting disc of $\sim 40 \, M_\odot$. Compared with these protostellar cores, it is expected that the core C-1A can potentially host a massive O/B-type star(s). Theoretical studies suggest that in the case of compact cores, the
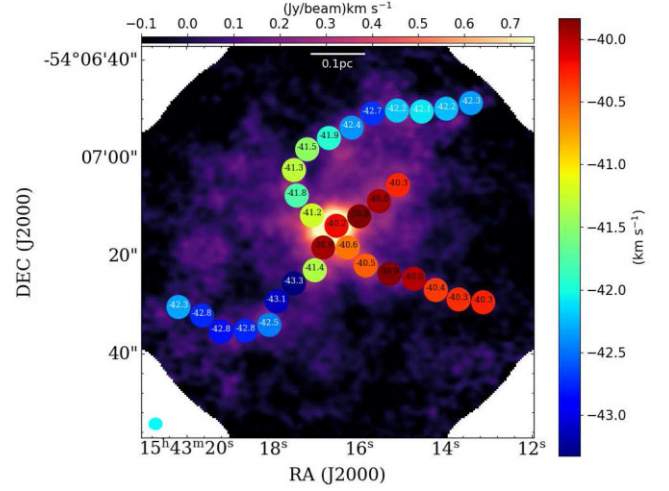

Figure 17. The background image is the moment0 map of the $H^{13}CO^+$ molecular line transitions. LSR velocities obtained within circular regions (2.5 arcsec), equivalent to the beam size, are overplotted on the image. The colour coding of the circles represents the variation in LSR velocities. The colour bar of the variation is also shown in the plot. The scale bar is shown on the top, and the beam size is shown in the bottom left corner.
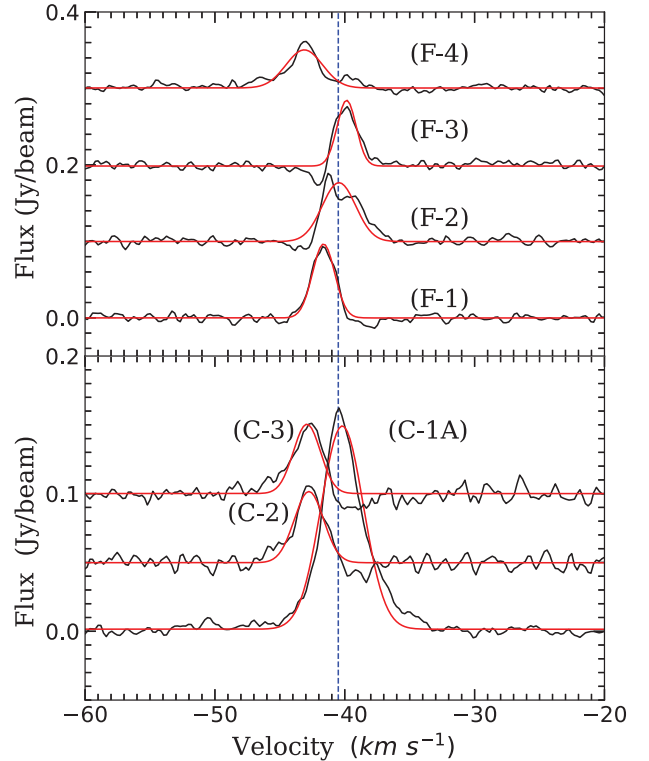

Figure 18. $H^{13}CO^+$ average spectra for the cores C-1A, C-2, and C-3 and over all filaments. The spectra are taken within the boxes shown in Fig. 8. Gaussian fits to all spectra are shown as red curves. Spectras of C-2, C-3, and filaments F2 to F4 are scaled up for a better representation. The vertical blue dashed line shows the LSR velocity of the central core.

amount of matter accreted onto the star is ∼ 50 per cent of the core mass (McKee & Tan 2003). We have to take into account the uncertainty (see Section 3.1.4) involved in mass estimations of the cores. With the uncertainty and also taking into consideration the unresolved components within, it is possible that core C-1A can potentially form a cluster with at least one single massive star with mass greater than 8 − 10 M$_\odot$.

Except for C-1B and C-1C, all other cores associated with IRAS 15394−5358 are more massive than 8 M$_\odot$. As depicted in Fig. 16, all the cores except C-1C lie outside the low-mass star-forming zone and meet the criterion of m(r) > 870M$_\odot$(r/pc)$^{1.33}$ (Kauffmann et al. 2010), suggesting that these cores might foster the formation of massive stars within themselves. As discussed earlier, compact cores typically utilize a significant fraction of their mass to form the most massive object. Cores C-2 and C-3 have masses of ∼17 M$_\odot$. Taking into account the uncertainty in mass along with unresolved components into consideration, it is likely that the cores can potentially form a cluster of low or intermediate mass stars. Similarly, the remaining cores, C-1B, C-1C, and C-4, have masses of 7, 3.4, and 9 M$_\odot$, respectively, and it is highly likely that low-mass stars will form within these cores. Consequently, the region of IRAS 15394−5358 is likely evolving into a stellar cluster, where the most massive member could potentially be a massive O/B-type star.

5 DISCUSSION

5.1 Mass transfer to the central hub

We detect a network of four filaments extending from the massive central core, thus creating a hub-filament system. As discussed earlier, in such a system, the hub serves as a progenitor for the formation of massive stars, where the filaments help in funnelling matter into the hub (Peretto et al. 2013; Chen et al. 2019; Chung et al. 2019, 2021; Liu et al. 2023). Here, we attempt to study any such mass infall into the central hub through the filaments.

We observe a velocity gradient in the protocluster region (Sections 3.2.6 and 3.2.7). To further explore the velocity gradient along the filaments, we extract H^{13}CO$^+$ average spectra within circular regions (2.5 arcsec) equivalent to the beam size. In Fig. 17, we provide the LSR velocity values obtained from the H^{13}CO$^+$ average spectra within the circular regions. The LSR velocities' distribution also reveals the velocity gradient along the filaments. Also, we extract spectra within the rectangular boxes shown in Fig. 8 to analyse such infall signatures within the region. In Fig. 18 we show the H^{13}CO$^+$ spectral profile of cores C-1A, C-2, and C-3. Also, we plot the average spectra taken over rectangular regions on all the filaments. It is interesting to notice that the velocity of filaments F1 and F4 are shifted to the lower side of C-1A, or they are blueshifted, and the filaments F2 and F3 are shifted to the higher side of C-1A or they are redshifted. The shift (∼ 3 km s^{-1}) of filament F4 is highest compared to all other filaments. The LSR velocities of the filaments F1 and F4 differ by ∼ 2 − 3 km s^{-1} from the systemic velocity, whereas it is ∼ 1 km s^{-1} for filaments F2 and F3. This suggests that more matter might be funnelled to the hub by F1 and F4 compared to the filaments F2 and F3. This further supports the fact that the observed velocity gradient is due to gas inflow to the central hub, as indicated by the PV map (Fig. 13). In the protocluster region SDC 335, Peretto et al. (2013) have observed a similar mass inflow to the hub from its surroundings and with high-resolution data Xu et al. (2023) observed the presence of condensations within the massive

core MM1 of the source SDC 335. All condensations can grow due to the mass infall into the central hub. In our case, further deep, higher resolution data would enable us to observe the presence of condensations within the central hub C-1/core C-1A and their mass accretion features.

It is clear that an active mass transfer is happening to the central hub C-1 from its surroundings. This is also evident in moment2 map (Fig. 11b), where the central hub region has higher velocity dispersion compared to its surroundings. The value is ∼ 2 km s^{-1}, and we assume it as the infall rate (V$_{in}$) to make an empirical estimate of mass accretion rate in the protocluster region of IRAS 15394−5358. Using the expression $\dot{M}_{in} = 3V_{in}^3/2G$ (Pineda et al. 2012), we obtain the mass infall rate to be 3×10^{-3} M$_\odot$ yr^{-1}. Assuming a typical free-fall time-scale of 5×10^4 yr (Rosen et al. 2019), the mass infall rate can collect matter of 150 M$_\odot$ in the central hub. This accretion is enough to gather matter similar to the mass of hub C-1 over a few free-fall times. This suggests that most of the central hub's mass is collected through a large-scale molecular cloud collapse over a few free-fall times. A simulation study by Schneider et al. (2010) also shows that such mass accumulation to the central hub is possible through a large parsec-scale molecular cloud collapse. Note that a better estimation of infall velocity is essential to derive the mass accretion rate in the complex.

5.2 Driving mechanism for massive star formation in IRAS 15394−5358

In the introduction, we discuss the several models proposed to understand the massive star formation process. Our kinematic analysis using the ATOMS data helps us to shed light on the possible driving mechanism at work for massive star formation in the protocluster complex IRAS 15394−5358. A hub-filament system is seen in the protocluster complex, where four filaments are linked with the hub. A velocity gradient is seen from the surroundings towards the centre, indicating a collective mass inflow towards the hub. In this section, we discuss the possible mechanisms at work for massive star formation in the protocluster.

All the dense cores of the protocluster complex have low virial parameters ($\alpha_{vir} < 1$), suggesting they are gravitationally bound in nature. Competitive accretion would be possible for a case of $\alpha_{vir} < 1$ (Krumholz, McKee & Klein 2005). Also, this model requires global hierarchical collapse (Ballesteros-Paredes et al. 2011; Vázquez-Semadeni et al. 2017) assuming initial fragmentation of a molecular cloud into Jeans core masses. The cores near the gravitational potential minimum are favoured with higher mass accretion. In the protocluster, the most massive core (C-1A) is present within the hub, and its location could be the primary reason for its higher mass compared to other dense cores of the complex. Also, it is observed that the other two dense cores, C-2 and C-3, with masses of ∼17 M$_\odot$, are present on the filament F4, which has the maximum velocity gradient among all the filaments. This higher velocity gradient might have helped to form these cores by supplying enough material. This morphology also supports the role of the GHC model, where multiscale infall motions are possible, with varying velocity gradients along filaments at different scales. The IF model suggests large-scale, converging, inertial flows occurring due to turbulence. Both the GHC and IF models predict very small velocity gradients (< 5 km s^{-1} pc^{-1}) at large scales (> 1 pc). A recent study of 26 IRDC clouds reports that the majority of these clouds are self-gravitating, ranging from tenths of a parsec to several tens of parsecs (Peretto et al. 2023), thereby questioning the importance of IF model in star formation. However, further studies are needed to

deepen our understanding of the role of these models in massive star formation.

At scales smaller than ~ 1 pc in the hub-filament systems, the longitudinal flow along the filaments can be attributed to GHC model. At such small scales, it is more likely that the infall will be primarily dominated by the gravity of the hub (Zhou et al. 2022). Similar results were also seen in a few previous studies (Liu et al. 2022a, b; Saha et al. 2022; Pan et al. 2024). In IRAS 15394−5358, the velocity gradient observed is ~ 20 km s^{-1} pc^{-1}, comparable with the values observed in massive star-forming regions at smaller scales (< 1 pc). This suggests competitive accretion, along with the GHC model, could be playing significant roles in the star-formation activity within the protocluster. Due to the large statistically significant sample size, the ATOMS survey can help us to gain more knowledge regarding inflow properties and the role of gravity/turbulence in massive star formation by characterizing the gas environment of hub-filament systems.

6 SUMMARY

Using the dust continuum and multiple molecular line transitions data from the ATOMS survey, we conducted a detailed analysis of the massive protocluster IRAS 15394−5358, where clump fragmentation and indications of massive star formation through a large-scale collapse have been observed. Significant findings of this work are the following.

(i) The 3 mm dust continuum map shows the fragmentation of the massive clump, revealing six cores within it. The dense central part, called core C-1, with a derived mass of 214 M$_\odot$, has three substructures called cores C-1A, C1-B, and C-1C. There are three other cores labelled as C-2, C-3, and C-4. Among all the cores, C-1A is the largest (radius $= 0.04$ pc), massive (157 M$_\odot$), and dense ($\Sigma = 8.6$ g cm^{-2}).

(ii) Two 24 µm blobs are seen towards the massive clump. The dense central part is associated with the less bright 24 µm blob, EGOs, and a methanol maser. The brighter 24 µm blob is associated with cores C-2 and C-3. This suggests that the dense central region hosts massive star formation and is likely at an early evolutionary stage compared to the surrounding cores.

(iii) Virial analysis reveals that all the cores are gravitationally bound. Our analysis shows that the protocluster region's fragmentation might have occurred at an earlier time following a thermal Jeans fragmentation process. Except for cores C-1B, C-1C, and C-4, all other cores might form a massive star. The massive core C-1A is prone to form a single massive O/B-type star.

(iv) The multiple line transitions of the protocluster region display different morphological features. Our PCA analysis shows that the molecular transitions can be broadly segregated into three groups. The first group contains H^{13}CN, H^{13}CO$^+$, HC$_3$N, and SO, the second group contains HCN, HCO$^+$, CCH, SiO, and CS, and the third group includes CH$_3$OH.

(v) Using the H^{13}CO$^+$ line, a hub-filament system was identified in IRAS 15394−5358, where the central hub is linked with four filaments labelled as F1 to F4. The H^{13}CO$^+$ moment1 and moment2 reveal the velocity gradient from the surrounding towards the hub. An average velocity gradient of ~ 20 km s^{-1} pc^{-1} is observed towards the hub from the surrounding regions. This supports a global collapsing scenario, where the filaments, primarily F1 and F4, are contributing to the hub through gas inflow. H^{13}CO$^+$ moment2 map reveals an enhanced line-width value (~ 1.8 km s^{-1}) towards the

hub, suggesting the ongoing star-forming activity in the dense central region.

(vi) Assuming the infall velocity to be 2 km s^{-1} same as the velocity dispersion in the central hub, we derive an empirical mass accretion rate of 3×10^{-3} M$_\odot$ yr^{-1}. This accretion rate would be enough to gather mass equivalent to the hub (C-1) in a few free-fall times. Considering the morphology of the dense cores distribution and velocity gradient, we speculate that competitive accretion along with GHC model might be at work for star formation activity in IRAS 15394−5358.

DATA AVAILABILITY

The data underlying this article can be shared on reasonable request to the PI of the ATOMS survey, Tie Liu (liutiepku@gmail.com).

REFERENCES

Anderson M. et al., 2021, MNRAS, 508, 2964

Arzoumanian D. et al., 2022, A&A, 660, A56

Ballesteros-Paredes J., Hartmann L. W., Vázquez-Semadeni E., Heitsch F., Zamora-Avilés M. A., 2011, MNRAS, 411, 65

Baug T. et al., 2018, ApJ, 852, 119

Benjamin R. A. et al., 2003, PASP, 115, 953

Bertoldi F., McKee C. F., 1992, ApJ, 395, 140

Bonnell I. A., Bate M. R., Clarke C. J., Pringle J. E., 2001, MNRAS, 323, 785

Bonnell I. A., Vine S. G., Bate M. R., 2004, MNRAS, 349, 735

Bontemps S., Motte F., Csengeri T., Schneider N., 2010, A&A, 524, A18

Bronfman L., Nyman L. A., May J., 1996, A&AS, 115, 81

Caratti o Garatti A., Stecklum B., Linz H., Garcia Lopez R., Sanna A., 2015, A&A, 573, A82

Caswell J. L., 1998, MNRAS, 297, 215

Chen H.-R. V. et al., 2019, ApJ, 875, 24

Chung E. J. et al., 2019, ApJ, 877, 114

Chung E. J. et al., 2021, ApJ, 919, 3

Contreras Y. et al., 2018, ApJ, 861, 14

Cyganowski C. J. et al., 2008, AJ, 136, 2391

Devereux N. A., Young J. S., 1990, ApJ, 359, 42

Dewangan L. K., Ojha D. K., Sharma S., Palacio S. d., Bhadari N. K., Das A., 2020, ApJ, 903, 13

Draine B. T., 2011, Physics of the Interstellar and Intergalactic Medium. Princeton Univ. Press, Princeton

Dunham M. M., Crapsi A., Evans N. J. II, Bourke T. L., Huard T. L., Myers P. C., Kauffmann J., 2008, ApJS, 179, 249

Elia D. et al., 2017, MNRAS, 471, 100

Faúndez S., Bronfman L., Garay G., Chini R., Nyman L. Å., May J., 2004, A&A, 426, 97

Garay G., Brooks K. J., Mardones D., Norris R. P., 2006, ApJ, 651, 914

Garay G., Mardones D., Brooks K. J., Videla L., Contreras Y., 2007, ApJ, 666, 309

Ginsburg A., Sokolov V., de Val-Borro M., Rosolowsky E., Pineda J. E., Sipőcz B. M., Henshaw J. D., 2022, AJ, 163, 291

Gómez G. C., Vázquez-Semadeni E., 2014, ApJ, 791, 124

Hacar A., Clark S. E., Heitsch F., Kainulainen J., Panopoulou G. V., Seifried D., Smith R., 2023, in Inutsuka S., Aikawa Y., Muto T., Tomida K., Tamura M., eds, ASP Conf. Ser. Vol. 534, Protostars and Planets VII. Astron. Soc. Pac., San Francisco. p. 153

He Y.-X. et al., 2023, ApJ, 957, 61

Heiderman A., Evans N. J. II, Allen L. E., Huard T., Heyer M., 2010, ApJ, 723, 1019

Henshaw J. D., Caselli P., Fontani F., Jiménez-Serra I., Tan J. C., 2014, MNRAS, 440, 2860

Hwang J. et al., 2022, ApJ, 941, 51

Issac N., Tej A., Liu T., Varricatt W., Vig S., Ishwara Chandra C. H., Schultheis M., 2019, MNRAS, 485, 1775

Jones P. A. et al., 2012, MNRAS, 419, 2961

Jones P. A., Burton M. G., Cunningham M. R., Tothill N. F. H., Walsh A. J., 2013, MNRAS, 433, 221

Kauffmann J., Bertoldi F., Bourke T. L., Evans N. J. II, Lee C. W., 2008, A&A, 487, 993

Kauffmann J., Pillai T., Shetty R., Myers P. C., Goodman A. A., 2010, ApJ, 716, 433

Kauffmann J., Pillai T., Goldsmith P. F., 2013, ApJ, 779, 185

Kirk H., Myers P. C., Bourke T. L., Gutermuth R. A., Hedden A., Wilson G. W., 2013, ApJ, 766, 115

Koch E. W., Rosolowsky E. W., 2015, MNRAS, 452, 3435

Krumholz M. R., McKee C. F., 2008, Nature, 451, 1082

Krumholz M. R., McKee C. F., Klein R. I., 2005, Nature, 438, 332

Kumar M. S. N., Palmeirim P., Arzoumanian D., Inutsuka S. I., 2020, A&A, 642, A87

Lada C. J., Lombardi M., Alves J. F., 2010, ApJ, 724, 687

Li G.-X., 2024, MNRAS, 528, 7333

Li S. et al., 2020, ApJ, 896, 110

Li G.-X., Cao Y., Qiu K., 2021, ApJ, 916, 13

Li S. et al., 2022, ApJ, 926, 165

Li S. et al., 2023, ApJ, 949, 109

Lin Z.-Y. D., Lee C.-F., Li Z.-Y., Tobin J. J., Turner N. J., 2021, MNRAS, 501, 1316

Liu H. B., Quintana-Lacaci G., Wang K., Ho P. T. P., Li Z.-Y., Zhang Q., Zhang Z.-Y., 2012, ApJ, 745, 61

Liu T. et al., 2016, ApJ, 824, 31

Liu H.-L., Stutz A., Yuan J.-H., 2019, MNRAS, 487, 1259

Liu T. et al., 2020, MNRAS, 496, 2790

Liu H.-L. et al., 2021, MNRAS, 505, 2801

Liu H.-L. et al., 2022a, MNRAS, 510, 5009

Liu H.-L. et al., 2022b, MNRAS, 511, 4480

Liu H.-L. et al., 2023, MNRAS, 522, 3719

Lo N. et al., 2009, MNRAS, 395, 1021

Lu X. et al., 2018, ApJ, 855, 9

Lumsden S. L., Hoare M. G., Urquhart J. S., Oudmaijer R. D., Davies B., Mottram J. C., Cooper H. D. B., Moore T. J. T., 2013, ApJS, 208, 11

Mai X. et al., 2024, ApJ, 961, L35

Marsh K. A., Whitworth A. P., Lomax O., 2015, MNRAS, 454, 4282

Marsh K. A. et al., 2017, MNRAS, 471, 2730

Mauch T., Murphy T., Buttery H. J., Curran J., Hunstead R. W., Piestrzynski B., Robertson J. G., Sadler E. M., 2003, MNRAS, 342, 1117

McClure-Griffiths N. M., Dickey J. M., Gaensler B. M., Green A. J., Haverkorn M., Strasser S., 2005, ApJS, 158, 178

McKee C. F., Tan J. C., 2003, ApJ, 585, 850

Molinari S. et al., 2010, PASP, 122, 314

Molinari S. et al., 2016, A&A, 591, A149

Morii S. et al., 2024, ApJ, 966, 171

Motte F., Bontemps S., Louvet F., 2018, ARA&A, 56, 41

Neelamkodan N., Tokuda K., Barman S., Kondo H., Sano H., Onishi T., 2021, ApJ, 908, L43

Olguin F. A. et al., 2021, ApJ, 909, 199

Olguin F. A., Sanhueza P., Ginsburg A., Chen H.-R. V., Zhang Q., Li S., Lu X., Sakai T., 2022, ApJ, 929, 68

Olguin F. A. et al., 2023, ApJ, 959, L31

Ossenkopf V., Henning T., 1994, A&A, 291, 943

Padoan P., Pan L., Juvela M., Haugbølle T., Nordlund Å., 2020, ApJ, 900, 82

Palau A. et al., 2015, MNRAS, 453, 3785

Pan S., Liu H.-L., Qin S.-L., 2024, ApJ, 960, 76

Peretto N., Hennebelle P., André P., 2007, A&A, 464, 983

Peretto N. et al., 2013, A&A, 555, A112

Peretto N., Rigby A. J., Louvet F., Fuller G. A., Traficante A., Gaudel M., 2023, MNRAS, 525, 2935

Peters T. et al., 2017, MNRAS, 467, 4322

Pineda J. E. et al., 2012, A&A, 544, L7

Pollack J. B., Hollenbach D., Beckwith S., Simonelli D. P., Roush T., Fong W., 1994, ApJ, 421, 615

Potdar A., Das S. R., Issac N., Tej A., Vig S., Chandra C. H. I., 2022, MNRAS, 510, 658

Ragan S. et al., 2012, A&A, 547, A49

Rathborne J. M., Garay G., Jackson J. M., Longmore S., Zhang Q., Simon R., 2011, ApJ, 741, 120

Rebolledo D. et al., 2020, ApJ, 891, 113

Redaelli E., Bovino S., Sanhueza P., Morii K., Sabatini G., Caselli P., Giannetti A., Li S., 2022, ApJ, 936, 169

Rigby A. J. et al., 2024, MNRAS, 528, 1172

Rosen A. L., Li P. S., Zhang Q., Burkhart B., 2019, ApJ, 887, 108

Rosolowsky E. W., Pineda J. E., Kauffmann J., Goodman A. A., 2008, ApJ, 679, 1338

Roy A. et al., 2014, A&A, 562, A138

Saha A. et al., 2022, MNRAS, 516, 1983

Sanhueza P., Jackson J. M., Zhang Q., Guzmán A. E., Lu X., Stephens I. W., Wang K., Tatematsu K., 2017, ApJ, 841, 97

Sanhueza P. et al., 2019, ApJ, 886, 102

Sanhueza P. et al., 2021, ApJ, 915, L10

Scalise E., Jr, Rodriguez L. F., Mendoza-Torres E., 1989, A&A, 221, 105

Schneider N., Csengeri T., Bontemps S., Motte F., Simon R., Hennebelle P., Federrath C., Klessen R., 2010, A&A, 520, A49

Schuller F. et al., 2009, A&A, 504, 415

Seshadri A., Vig S., Ghosh S. K., Ojha D. K., 2024, MNRAS, 527, 4244

Shimajiri Y. et al., 2017, A&A, 604, A74

Shirley Y. L., 2015, PASP, 127, 299

Shirley Y. L., Huard T. L., Pontoppidan K. M., Wilner D. J., Stutz A. M., Bieging J. H., Evans N. J. II, 2011, ApJ, 728, 143

Shu F. H., Adams F. C., Lizano S., 1987, ARA&A, 25, 23

Smith R. J., Glover S. C. O., Klessen R. S., Fuller G. A., 2016, MNRAS, 455, 3640

Smith R. J. et al., 2020, MNRAS, 492, 1594

Stutz A. M., Gould A., 2016, A&A, 590, A2

Tokuda K. et al., 2019, ApJ, 886, 15

Treviño-Morales S. P. et al., 2019, A&A, 629, A81

Urquhart J. S. et al., 2007, A&A, 474, 891

Urquhart J. S. et al., 2014, MNRAS, 443, 1555

Urquhart J. S. et al., 2018, MNRAS, 473, 1059

Vázquez-Semadeni E., Gómez G. C., Jappsen A. K., Ballesteros-Paredes J., Klessen R. S., 2009, ApJ, 707, 1023

Vázquez-Semadeni E., González-Samaniego A., Colín P., 2017, MNRAS, 467, 1313

Vázquez-Semadeni E., Palau A., Ballesteros-Paredes J., Gómez G. C., Zamora-Avilés M., 2019, MNRAS, 490, 3061

Vázquez-Semadeni E., Gómez G. C., González-Samaniego A., 2024, MNRAS, 530, 3445

Vázquez-Semadeni E. et al., 2024, preprint (arXiv:2408.10406)

Vuong M. H., Montmerle T., Grosso N., Feigelson E. D., Verstraete L., Ozawa H., 2003, A&A, 408, 581

Wang P., Li Z.-Y., Abel T., Nakamura F., 2010, ApJ, 709, 27

Wang K., Zhang Q., Wu Y., Zhang H., 2011, ApJ, 735, 64

Wang K. et al., 2014, MNRAS, 439, 3275

Xu F.-W. et al., 2023, MNRAS, 520, 3259

Xu F. et al., 2024, ApJS, 270, 9

Yang D. et al., 2023, ApJ, 953, 40

Young C. H., Evans N. J. II, 2005, ApJ, 627, 293

Yuan J. et al., 2018, ApJ, 852, 12

Zapata L. A., Ho P. T. P., Schilke P., Rodríguez L. F., Menten K., Palau A., Garrod R. T., 2009, ApJ, 698, 1422

Zhang Q., Wang K., Lu X., Jiménez-Serra I., 2015, ApJ, 804, 141

Zhang C. et al., 2023, MNRAS, 520, 3245

Zhou J.-W. et al., 2022, MNRAS, 514, 6038

Zhou J. W. et al., 2023, A&A, 676, A69

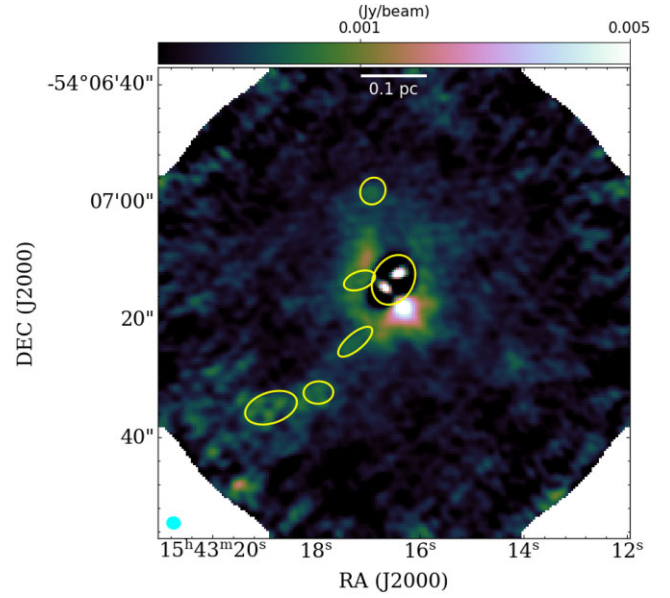# APPENDIX A: 3 MM CONTINUUM RESIDUAL MAP

Figure A1. The 3 mm continuum residual map retrieved from CASA *imfit* task while obtaining the core properties (see Section 3.1.2).

This paper has been typeset from a TEX/LATEX file prepared by the author.